Geostrophic Velocity Measurement Techniques for the Meridional Overturning Circulation and Meridional Heat Transport in the South Atlantic*

Renellys C. Perez†

Cooperative Institute for Marine and Atmospheric Studies, University of Miami, Miami, FL

NOAA/Atlantic Oceanographic and Meteorological Laboratory, Miami, FL

Silvia L. Garzoli, Christopher S. Meinen,

NOAA/Atlantic Oceanographic and Meteorological Laboratory, Miami, FL

Ricardo P. Matano

Oregon State University, College of Oceanic and Atmospheric Sciences, Corvallis, OR

*Atlantic Oceanographic and Meteorological Laboratory Contribution Number xxxx.

†*Corresponding author address:* Renellys C. Perez, Cooperative Institute for Marine and Atmospheric Studies, University of Miami, 4600 Rickenbacker Causeway, Miami, FL 33149.

E-mail: Renellys.C.Perez@noaa.gov

ABSTRACT

Two ocean general circulation models are used to test the ability of geostrophic velocity measurement systems to observe the Meridional Overturning Circulation (MOC) and meridional heat transport (MHT) in the South Atlantic. Model sampling experiments are conducted at five latitudes (between 15°S and 34.5°S) spanning the range of extratropical current regimes in the South Atlantic. Two methods of estimating geopotential height anomalies and geostrophic velocities are tested, simulating dynamic height moorings (T, S array) and current and pressure recording inverted echo sounders (CPIES array) deployed within the models. The T, S array accurately reproduces the MOC variability with a slight preference for higher latitudes, while the CPIES array has skill only at higher latitudes due to the increased geopotential height anomaly signal. Whether direct model velocities or geostrophic velocities are used, MHT and the MOC are strongly correlated, and successful reconstruction of MHT only occurs when there is skill in the MOC reconstructions. The geopotential height anomaly signal is concentrated near the boundaries along 34.5°S suggesting that this is an advantageous latitude for deployment of an *in situ* array. Four reduced arrays that build upon the sites from two existing pilot arrays along 34.5°S were examined. For these realistically-sized arrays, the MOC and MHT reconstructions from the T, S and CPIES arrays have comparable skill, and an array of approximately 20 instruments can be effectively used to reproduce the temporal evolution and vertical structure of the MOC and MHT.

1. Introduction

The Atlantic component of the meridional overturning circulation (MOC) includes the sinking of surface waters at higher latitudes in the North Atlantic, meridional translation of these deep waters and other remotely formed water masses around the world, gradual upwelling, and a return to the deep water formation regions through the South Atlantic. This overturning circulation is composed of wind-driven transports and the buoyancy-forced thermohaline circulation (Lee and Marotzke 1998). To compute the strength of the MOC in an ocean basin along a line of constant latitude, one needs to measure the total meridional flow across the line. Practically, to do this geostrophic velocity measurement techniques are employed (e.g, geostrophic currents are computed from zonal sections of density profiles and bottom velocity measurements), and are combined with zonal wind stress measurements across the basin. Unfortunately, cross-basin measurements suitable to estimate geostrophic transport have historically been limited to a few hydrographic sections (e.g., Ganachaud and Wunsch 2000; Ganachaud 2003; Lumpkin and Speer 2007) that at best provide snapshots of the MOC, from which it is challenging and controversial to assess long-term variations and trends (e.g., Bryden et al. 2005; Cunningham et al. 2007; Kanzow et al. 2010).

At present the only existing time series of basin-wide MOC transport is in the subtropical North Atlantic. With the inception of the Rapid Climate Change/Meridional Overturning Circulation and Heat Flux Array (RAPID/MOCHA) array along 26.5°N in April 2004, continuous-in-time estimates of the MOC and meridional heat transport (hereafter MHT) are now available. The RAPID/MOCHA array, coupled with the long-term NOAA Western Boundary Time Series (WBTS) program in the Florida Straits and east of the Bahamas,

merges *in situ* data from dynamic height moorings (tall moorings with temperature, salinity and pressure recorders) augmented with current meters, pressure equipped inverted echo sounders (PIES), PIES augmented with current meters 50 m above the seafloor (CPIES), and a submarine telephone cable, with satellite-based wind measurements (e.g., Baringer and Larsen 2001; Meinen et al. 2006; Cunningham et al. 2007). Model-based sampling experiments using geostrophic velocity measurement techniques were first conducted prior to the deployment of this basin-wide MOC observing system (Hirschi et al. 2003).

The limited collection of hydrographic sections in the South Atlantic has hampered efforts to understand the impact of the South Atlantic on the global MOC. Models and observations suggest that the South Atlantic is not a passive conduit for remotely formed water masses associated with the MOC, such as Antarctic Bottom Water and Circumpolar Deep Water (e.g., Hogg et al. 1999; Zenk et al. 1999), and that it actively participates in water mass transformations, particularly in regions of high meoscale variability such as the Brazil/Malvinas Confluence and at the Agulhas Retroflection (Schouten and Matano 2006, Jullion et al. 2010; Garzoli and Matano 2011 and references therein). Models and observations also show that the South Atlantic plays a significant role in the establishment of oceanic teleconnections (e.g., Speich et al. 2007). This highlights the need for sustained observations in the South Atlantic, which, in conjunction with modeling efforts, would improve understanding of the processes necessary to formulate long-term climate predictions. The U.S. Climate Variability and Predictability Research Program (CLIVAR) Atlantic MOC (AMOC) implementation strategy calls for a MOC and MHT monitoring array across the South Atlantic (http://www.usclivar.org/plans.php), and three South Atlantic MOC (SAMOC) workshops have been held to design the basis for an observational program (Garzoli et al. 2010). At the

conclusion of the SAMOC 3 workshop, it was proposed to instrument and sustain a zonal trans-basin South Atlantic array that will, together with ongoing studies across the two Southern Ocean choke points (Drake Passage and the GoodHope line south of South Africa) and the RAPID/MOCHA array at 26.5°N, provide measurements to evaluate inter-gyre, inter-hemispheric, and inter-ocean connectivity of the MOC (Garzoli et al. 2010).

To date, model studies have provided some guidance on a suitable location for a zonal trans-basin *in situ* array in the South Atlantic. A model study by Sime et al. (2006) using the coupled global climate model HadCM3 found that hydrographic sections unsupported by bottom pressure or bottom velocity information or wind information would best reconstruct the MOC around 25°S. Model-based sampling experiments by Baehr et al. (2009) using the global climate model ECHAM5/MPI-OM suggested that 18°S would be a suitable latitude to sample the MOC in the South Atlantic with geostrophic velocity measurement techniques unsupported by bottom velocity information but supported by wind information. However, the ocean component of the coupled models used in those studies were too coarse (horizontal resolution of 1.25° or greater) to adequately resolve western boundary currents. A yet unpublished study by researchers at the University of Southampton using both a coarse (1/4°) and high (1/12°) resolution version of the global ocean model OCCAM finds that a geostrophic velocity measurement system, unsupported by bottom velocity measurements but supported by wind information, produced the least biased estimate of the MOC but poorly captured the variability along 25°S, whereas an observing system along 15°S or between 32°S and 34.5°S would best capture the MOC variability (E. McDonagh and P. Abrahamsen, personal communication). Due to the large spread in suggested latitudes (15°S to 34.5°S) and the assumed constraint of zero bottom velocity in previous studies, further analysis is needed to

determine a suitable latitude for a South Atlantic array.

In this paper, numerical simulations from two ocean general circulation models, the Parallel Ocean Climate Model (POCM) and the Ocean general circulation model For the Earth Simulator (OFES), are used to test the ability of *in situ* geostrophic velocity measurement systems supported by bottom velocity information and wind information to observe the MOC and MHT in the South Atlantic. Geostrophic velocity measurement techniques are horizontally integrating by nature, whereas a "picket fence" of direct velocity measurements and bottom pressure recorders require that moorings be spaced closer than zonal decorrelation length scales and as such are logistically unfeasible for a fully resolved basin-wide array. Model sampling experiments are conducted to test whether five latitudes, 15°S, 20°S, 25°S, 30°S, and 34.5°S (black lines in Fig. 1), are well suited for the deployment of a basin-wide South Atlantic array. The southernmost latitude 34.5°S is the southern boundary of the Atlantic and samples across the southward flowing Brazil Current, northward flowing Benguela Current and Agulhas Eddy corridor in both models, and the northernmost latitude 15°S is well outside of the equatorial waveguide and samples across the northward flowing North Brazil Current in both models (Fig. 1b). These five latitudes are also examined because they encompass locations suggested as suitable for an array in previous studies, or coincide with existing observing systems: 30°S (CLIVAR A10 trans-basin hydrographic sections) and 34.5°S (quarterly AX18 high-density XBT sections since 2002, and two pilot arrays of PIES/CPIES deployed near western and eastern boundaries by an international consortium including the United States, France, Argentina, South Africa, and Brazil).

The paper outline is as follows: A description of the models and the method used to reconstruct the MOC and MHT signals with virtual arrays deployed within those models is

provided in section 2. The temporal and meridional scales of variability of the MOC and MHT and their interrelation are explored in section 3. In section 4, the ability to reconstruct these signals with geostrophic measurement techniques (i.e. dynamic height moorings with near-bottom velocity and pressure measurements) is examined. Such moorings are expensive, and in section 5, the ability to sample the MOC and MHT with CPIES is tested. In section 6, realistically-sized arrays (e.g., reasonable number of sites) are examined that build upon the existing sites from 34.5°S pilot arrays. Finally, in section 7, the results are discussed and summarized.

2. Models and Method

a. Models

Fields from two global eddy-permitting to eddy-resolving ocean simulations, POCM and OFES, are used to characterize the South Atlantic MOC and MHT. Both models reproduce most of the important aspects of the South Atlantic circulation with adequate realism (e.g., Fig. 1 shows the similarity between mean POCM and OFES meridional currents at 200 m depth), but they vary in the scales they resolve and in the complexity of their numerical schemes. While no model is perfect, concurrent analysis of two different simulations will reduce the uncertainties associated with using only one of them and additionally reveals whether geostrophic velocity measurement systems can capture two different realizations of volume and heat transport.

POCM 4C (hereafter POCM) is an implementation of the Semtner/Chervin primitive

equation, hydrostatic, z-level model (Semtner et al. 1992; Stammer et al. 1996; Tokmakian and Challenor 1999). The model equations have been discretized in a Mercator B-grid with a nominal horizontal resolution of 1/4° and 20 vertical z levels. POCM was forced with daily atmospheric fluxes from the European Center for Medium Weather Forecast (ECMWF) reanalysis starting from 1979 to 1994, and with operational ECMWF data sets until 1998 (Tokmakian and Challenor 1999). Although the full integration period was 19-years, only the last twelve years (1986-1997) are analyzed here (similar to Matano and Beier 2003; Schouten and Matano 2006; Baringer and Garzoli 2007; Garzoli and Baringer 2007; Fetter and Matano 2008). POCM results are available as 3-day averages every 9-days.

OFES is a massively-parallelized implementation of version 3 of the NOAA/GFDL Modular Ocean Model (MOM3) run by Japan Agency for Marine-Earth Science and Technology (JAMSTEC). The model equations have been discretized in a Mercator B-grid with a horizontal resolution of 0.1° and 54 vertical z levels. Note, model fields were provided by JAMSTEC at 0.2° increments (every other horizontal grid point). The simulation used in this study was spun up for 50-years with a monthly climatology derived from NCEP/NCAR reanalysis atmospheric fluxes (Masumoto et al. 2004), and then forced with daily mean NCEP/NCAR reanalysis data from 1950 to 2007 (Sasaki et al. 2008). Results are analyzed for the same twelve years as the POCM simulation. OFES results are available as snapshots at 3-day intervals.

POCM has been compared against available observations (Stammer et al. 1996; Tokmakian and Challenor 1999; Matano and Beier 2003; Schouten and Matano 2006; Fetter and Matano 2008) and has well-known strengths and weaknesses. Matano and Beier (2003) found that large-scale circulation patterns reproduced by POCM agree well with those in-

ferred from hydrographic observations, except in the southeastern Atlantic at intermediate and deep levels. The path of the Agulhas rings in POCM are in close agreement with the path inferred from altimetric data, however eddy shedding is too infrequent in the model (Matano and Beier 2003). POCM successfully simulates the low-frequency variability of the ACC and the Malvinas Current, but it does not reproduce the correct location of the Brazil-Malvinas Confluence (Fetter and Matano 2008).

While output from OFES has contributed to many studies in the Pacific ocean, to date few published studies have looked at its behavior in the South Atlantic (Masumoto 2010; and references therein). OFES reproduces well the large-scale SSH variability in the South Atlantic compared with altimetric data (Dong et al. 2011; E. Giarolla, personal communication). However, OFES underestimates the quasi-decadal increasing tendency of SSHA observed in the South Atlantic (E. Giarolla, personal communication), and the Agulhas rings are too energetic and the Agulhas ring corridor extends too far to the north in the model (Dong et al. 2011; E. Giarolla, personal communication).

b. MOC and MHT calculation

Fields from both model simulations are used to construct estimates of the maximum northward volume transport in the upper limb of the overturning circulation (i.e., the MOC) and total MHT. The strength of the MOC is given by

$$MOC(t) = \int_{z=-D(t)}^{z=0} dz \int_{x=x_W}^{x=x_E} dx \; (v(t;x,z) + v_c(t)), \tag{1}$$

where $D(t)$ is the mid-ocean depth at which the basin-wide integrated volume transport switches from northward to southward (at approximately 1200 m in OFES and approximately 1500 m in POCM), $v(t;x,z)$ is the model meridional current, and $v_c(t)$ is a spatially uniform constant applied to give zero net volume transport (as described in Hall and Bryden 1982; Hirschi et al. 2003; Baehr et al. 2004). Total MHT is computed as

$$Q(t) = \int_{z=z_{btm}}^{z=0} dz \int_{x=x_W}^{x=x_E} dx \; \rho c_p T(t;x,z) v(t;x,z) \tag{2}$$

where $\rho = \rho(S,T,p)$ and $c_p = c_p(S,T,p)$ are computed from UNESCO (1983) equations of state using $S(t;x,z)$ and $T(t;x,z)$ from the model simulations and p evaluated at each model z-level. Note that the heat transport itself is not mass balance corrected (J. Hirschi, personal communication).

c. MOC reconstruction with geostrophic velocity measurement techniques

The zonal trans-basin arrays deployed within the high-resolution ocean simulations are assumed to provide geopotential height anomaly profiles (Φ_{array}) at every zonal grid point. Geostrophic velocity is then computed, $v_{g,array} = f^{-1}\partial\Phi_{array}/\partial x$, and used to reconstruct the MOC and MHT. Conceptually, this approach is similar to sampling experiments conducted by Hirschi et al. (2003) and Baehr et al. (2004) in the North Atlantic, and more recently by Baehr et al. (2009) in the South Atlantic. However, here the assumption of zero bottom velocity is relaxed, and reconstructions are compared from geopotential height anomalies derived from two different measurement techniques. First, model T, S profiles are directly

used to calculate geopotential height anomalies ($\Phi_{T,S}$) simulating the use of dynamic height moorings (e.g., Hirschi et al. 2003; Baehr et al. 2004; Baehr et al. 2009). Second, model T, S profiles are used to calculate a vertical sound speed profile, which is then integrated to obtain vertical acoustic travel time. Travel time is then related through look-up tables to geopotential height anomaly profiles (Φ_{CPIES}), simulating the use of CPIES. This indirect method is described in more detail in section 2d.

For both measurement systems, the reconstructed MOC is given by

$$MOC_{array}(t) = \int_{z=-D_{array}(t)}^{z=0} dz \int_{x=x_W}^{x=x_E} dx \; v'_{array}(t; x, z) \tag{3}$$

where

$$v'_{array}(t; x, z) = v_{g,array}(t; x, z) + v_b(t; x, z_{btm}) + v_{Ek}(t; x, z \geq -D_{Ek}) + v_{c,array}(t). \tag{4}$$

and is the sum of geostrophic velocity ($v_{g,array}$), bottom velocity (v_b), Ekman velocity (v_{Ek}), and the "zero-net-volume-transport" velocity correction ($v_{c,array}$), respectively. Only $v_{g,array}$ and $v_{c,array}$ vary depending on the use of $\Phi_{T,S}$ versus Φ_{CPIES}. Ekman transport is computed from the wind stress fields used to force each model simulation, and is evenly distributed in the upper 50 m ($D_{Ek} = 50\ m$).

In previous sampling studies, the assumption of zero bottom velocity $v_b(t) = 0$ led to errors in reproductions of the strength and variability of the MOC along latitudes with strong bottom trapped currents (Baehr et al. 2004; Baehr et al. 2009). Therefore, any

planned geostrophic velocity measurement system in the South Atlantic will make direct near-bottom velocity measurements with current meters 50 m above the seafloor and measure time-varying barotropic flow variations with bottom pressure recorders. For simulations of full trans-basin arrays in sections 4 and 5, v_b is taken directly from the model velocities at the greatest common depth between adjacent geopotential height anomaly profiles to reference the geostrophic velocity shear. For simulations of realistically-sized arrays where the spacing between moorings may exceed zonal decorrelation length scales in section 6, currents are zonally averaged between sites at the shallowest common depth level. This zonal-averaging simulates the type of information that zonal differences of bottom pressure data would provide about the time-varying barotropic flow combined with leveling/referencing by direct velocity measurements made near the base of the moorings (e.g., Johns et al. 2008). Velocity in cross-sectional area that lies below greatest common depth level is filled in with velocity from the adjacent offshore site and integrated over the "bottom triangle".

It should be noted that, as with previous array evaluation studies (e.g., Hirschi et al. 2003, Baehr et al. 2004, Baehr et al. 2009) not all aspects of the observing system design are being tested here. Evaluating different vertical distributions of "sensors" on a mooring and vertical blow-down of a mooring (both of which would require models with much finer vertical resolution), pressure sensor drift, and measurement errors are beyond the scope of this paper. Instead the focus is testing how well velocities computed from direct and indirect geostrophic-techniques can reconstruct the MOC and MHT.

d. Estimation of geopotential height anomalies from virtual CPIES

Vertical acoustic travel times τ computed from model hydrography are combined with look-up tables to produce time series of specific volume anomalies δ at each zonal gridpoint. Conceptually, this is similar to the way time series of δ profiles are obtained from CPIES deployed in the real ocean (Meinen and Watts 2000; Watts et al. 2001; Meinen et al. 2004; Meinen et al. 2006), with the difference of perfect knowledge of the model hydrography right at each grid point over the twelve year study period rather than hydrography from a limited number of CTD profiles spread throughout the study region. To construct the $\delta(\tau, p)$ look-up tables, δ profiles computed from model hydrography are sorted by their corresponding τ value and objectively mapped onto a uniform grid with 0.1 ms spacing, assuming a Gaussian covariance with a correlation length scale of 5 ms and a noise-to-signal energy ratio of 0.01 (Bretherton *et al.* 1976). Fig. 2a shows a sample $\delta(\tau, p)$ look-up table in OFES at a gridpoint on the western boundary, 34.5°S, 48°W. Using the table, a time series of δ_{CPIES} profiles is generated at this particular location. Fig. 2b shows the scatter of δ about δ_{CPIES} as a function of travel time at 500 *db*. Integration of the δ_{CPIES} profiles with respect to pressure yields geopotential height anomaly profiles Φ_{CPIES} (Fig. 2c) from which $v_{g,CPIES}$ is then computed. Look-up tables are also constructed for $T(\tau, p)$ and $S(\tau, p)$ for the heat flux reconstructions.

e. MHT reconstruction with geostrophic velocity measurement techniques

The reconstructed MHT is similar for the two arrays

$$Q_{array}(t) = \int_{z=z_{btm}}^{z=0} dz \int_{x=x_W}^{x=x_E} dx \; \rho c_p T(t;x,z)(v_{g,array}(t;x,z) + v_b(t;x,z_{btm})) + Q_{Ek}(t). \quad (5)$$

Here, it is assumed that there is perfect knowledge of the temporal evolution of T, S (and hence ρ and c_p) for $Q_{T,S}$ calculation, whereas T, S are reconstructed from look-up tables for the Q_{CPIES} calculation. Ekman heat transport, $Q_{Ek}(t)$, is computed using temperatures vertically averaged in the upper 50 m, and is evenly distributed in the upper 50 m.

3. Model MOC and MHT

a. MOC

The MOC time series calculated using (1) and direct model velocities from OFES and POCM are analyzed here. The MOC time series are quite consistent between OFES and POCM on annual to quasi-decadal timescales at all five latitudes (left panels of Fig. 3 and Table 1). Note that a 9-month frequency-domain low-pass filter was applied to the time series to focus on climate relevant time scales. The mean MOC strength ranges between 15.0 to 16.5 Sv (Table 1). In both models, northward transport increases by approximately 1 Sv from 34.5°S to 15°S. This increase in overturning strength from higher to lower latitudes is generally consistent with overturning transports inferred from global inversions of WOCE hydrographic sections, acknowledging the inversions have order 3 Sv error bars (e.g., Ganachaud 2003; Lumpkin and Speer 2007). In OFES, however, this increase is not monotonic, specifically there is a 0.5 Sv decrease in transport from 25°S to 20°S due to southward

flow in the semi-enclosed basin between the Brazilian coast and the Vitória-Trindade ridge (Fig. 1). Except at those two latitudes, inter-model biases are less than 0.2 Sv (Table 1). The right panels of Fig. 3 show that below the level of the maximum MOC transport (e.g., below 1500 m) the structure of the time-mean volume transport, $G_V(z)$, is very different between the two simulations. This is due to the relatively weak inflow of Antarctic Bottom Water in POCM that was previously diagnosed in Schouten and Matano (2006).

To examine how the MOC variance is distributed among different time-scales in both the OFES and POCM simulations (Fig. 4), the MOC time series has been partitioned into five distinct frequency bands: high-frequency (HF, periods less than 90 days), semi-annual (SA, 90 to 270 days), annual (A, 270 to 450 days), inter-annual (IA, 450 to 1260 days), and quasi-decadal (QD, periods greater than 1260 days). The total (or unfiltered) variance is also computed for both simulations (circles in Fig. 4a,b).

At all latitudes the total MOC variability is larger in OFES compared with POCM, due in part to the different model-archival frequencies and the eddy-resolving nature of OFES vs. eddy-permitting nature of POCM. The latter effect is most pronounced at higher latitudes (25°S to 34.5°S) where OFES is twice as energetic as POCM due mainly to the more frequent passage of strong Agulhas eddies in OFES. Consistent with this, high-frequency variability accounts for over 60% of the total MOC variance in OFES, but only about 50% of the total variance in POCM (Fig. 4c,d)[1]. There is a significant amount of energy at both semi-

[1]It has been shown that the 3-day snapshot sampling used by OFES misplaces the portion of the total variance related to the diurnal oscillation into the portion of the total variance related to the mean (Priestley 1981; von Storch et al. 2007), and as such the high-frequency variability shown here is underestimated by the variance associated with the diurnal cycle. Similarly, there may be 3-day variability aliased by the POCM

annual and annual time scales (Fig. 4a,b). In POCM, the semi-annual and annual variance are comparable at all latitudes, with more energy at annual time scales only along 15°S, 20°S and 34.5°S. In OFES, the annual variance dominates the semi-annual at 30°S and 34.5°S. The amplitude of the annual cycle of the MOC in these models is stronger than the amplitude of the MOC annual cycle found by Dong et al. (2009) along 34.5°S from 17 XBT transects collected along the AX18 line, but is consistent with the strong amplitude observed at the RAPID/MOCHA array at 26.5°N (Kanzow et al. 2010). Inter-annual and quasi-decadal variability account for less than 6% and 4%, respectively, of the total variance in both models, and is weakest at 30°S and 34.5°S in both models. If this holds true in the real ocean, an accurate representation of the MOC annual cycle will be crucial to assess long-term variations.

b. Meridional heat transport

As was the case for the MOC time series, there is general agreement between the time series of MHT between OFES and POCM on annual to quasi-decadal timescales with mean values between 0.41 PW and 0.55 PW (left panels of Fig. 5 and Table 2). The mean MHT increases in magnitude from 34.5°S to 15°S. However, the meridional gradient of $\overline{Q}$ is more pronounced in OFES which increases by 0.09 PW, while in POCM the increase is 0.04 PW (Table 2). Note that Lumpkin and Speer (2007) reported an 0.12 PW increase in MHT from 0.62 ± 0.15 PW at 32°S to 0.74 ± 0.36 PW at 11°S using inversions of hydrographic sections. The weak meridional gradient of $\overline{Q}$ in POCM and bias between the two models at

temporal sampling.

higher latitudes (right panels of Fig. 5 show $G_H(z)$ the time-mean of vertically integrated meridional heat transport) are due to the weaker meridional cell below the North Atlantic Deep Water cell (right panels of Fig. 3).

The distribution of MHT variance into different frequency bands is similar to the MOC variance breakdown shown in Fig. 4. This is evident from the high correlation between MHT and the MOC at all time scales considered here (Fig. 6a,b and Table 3). For example, when high-frequency and semi-annual time scales are excluded the correlation between MHT and the MOC ranges from 0.87 to 0.96 (Table 3). When Q is regressed onto the MOC strength, a robust linear relationship is found for all latitudes (Fig. 6c,d and Table 3). This relationship only begins to deteriorate on quasi-decadal time scales. At 34.5°S, the slope is around 0.05 $PWSv^{-1}$ for high-frequency to inter-annual time scales. These correlations and slopes are consistent with XBT based estimates along 34.5°S where a correlation of 0.76 and slope of 0.05 ± 0.01 $PWSv^{-1}$ were found (Dong et al. 2009). Linear regressions of the RAPID/MOCHA array data at 26.5°N reveal comparable slopes of 0.079 $PWSv^{-1}$ when MHT was regressed onto the total MOC and 0.064 $PWSv^{-1}$ when Ekman variability is removed prior to the regression (Johns et al. 2011).

4. Geostrophic estimation of the MOC and MHT

The MOC and MHT are first reconstructed using the full model T, S profiles at every zonal and vertical gridpoint ($MOC_{T,S}$ and $Q_{T,S}$, respectively) and compared with the "true" MOC and Q from section 3 to test along which latitudes geostrophic-type measurements will be most successful. The left panels of Fig. 7 demonstrate the skill of the MOC reconstructions

on annual to quasi-decadal time scales for OFES (black solid line) and POCM (blue solid line). The geostrophic technique applied to OFES is able to reproduce the mean MOC (compare black dashed and solid lines in Fig. 7a), with mean differences at five latitudes smaller than ± 0.7 Sv (black solid line in Fig. 7c). In contrast, the geostrophic technique has difficulty reconstructing the mean MOC in POCM at some latitudes due to weak mean ageostrophic currents on the western boundary (compare blue dashed and solid lines in Fig. 7a), with biases as large as 1.4 Sv at 30°S (blue solid line in Fig. 7c). Note that these departures from geostrophy may simply be an artifact of using 3-day averages of POCM T, S in the nonlinear dynamic height anomaly calculation.

In terms of accurately reproducing the variability of the MOC, the standard deviation of the difference between $MOC_{T,S}$ and MOC is smaller than 1 Sv everywhere for both simulations (Fig. 7e) and the correlation between $MOC_{T,S}$ and MOC is always greater than 0.9 (Fig. 7g). The reconstructions improve (i.e., lower standard deviation difference and slightly higher correlation) at higher latitudes where the Coriolis parameter is larger. In general, the reconstructions yield better results in OFES than in POCM (compare black and blue lines Fig. 7e,g).

The geostrophic technique applied to OFES is able to reproduce the mean MHT (compare black dashed and solid lines in Fig. 7b) with biases of 0.01 PW at 34.5°S and approximately 0.07 PW elsewhere (black solid line in Fig. 7d). In POCM, however, the geostrophic technique produces significantly biased estimates of MHT with biases larger than ± 0.10 PW at 20°S, 30°S, and 34.5°S (blue solid line in Fig. 7d). Because the MHT calculation is nonlinear and some temperature fluctuations may be uncorrelated with geostrophic currents, there is slightly less skill in the $Q_{T,S}$ reconstructions (Fig. 7f,h). The standard deviation of the dif-

ference between $Q_{T,S}$ and Q is fairly uniform in both models with values of around 0.03 PW in OFES and 0.07 PW in POCM, with the outlier being a standard deviation of 0.11 PW at 15°S in POCM (Fig. 7f). Correlation between $Q_{T,S}$ and Q is everywhere larger than 0.65, increases towards higher latitudes, and is larger in OFES than in POCM (Fig. 7h). Note that as expected, the spatial sampling at every other grid point of OFES fields (see section 2a) does not appreciably reduce the skill of the MOC or MHT reconstructions from geostrophic estimation techniques.

5. Simulating a CPIES measurement array

In the preceding section, it was established that the geostrophic estimation technique works well at all five latitudes and is able to reproduce the variability on annual to quasi-decadal time scales in both models. These initial tests are idealized, however, in the sense that they imply an array of perfect T, S measurements at every horizontal and vertical grid point. As such, the results from the preceding section provide a "best case" test of the performance for an array of dynamic height moorings (T, S array) of the type used in the RAPID/MOCHA array (e.g., Fig. 1b in Johns et al. 2008). In this section, we consider whether transports can be reconstructed using a trans-basin array of the more cost-effective CPIES. Because the narrative is similar for the OFES and POCM simulations (e.g., Table 4 compares signal-to-noise ratios of the CPIES reconstructions in both models), hereafter only results from the OFES analysis are discussed.

For both the T, S and CPIES array, geostrophic currents have similar means ($\overline{v}_{g,TS} \approx \overline{v}_{g,CPIES}$) and the same Ekman currents and bottom currents are applied in (4). Hence, the

bias between MOC_{CPIES} and MOC is essentially the same as for the T, S array (compare gray solid and black dashed lines in Fig. 8a). The MHT calculation in (5) is nonlinear and T, S are reconstructed from look-up tables. Consequently, the mean bias between Q_{CPIES} and Q does differ from that of the T, S array but is fairly uniform (0.05 PW) across the five latitudes (compare gray solid and black dashed lines in Fig. 8b).

In terms of variability, the standard deviation of $MOC_{CPIES} - MOC$ (black dashed line in Fig. 8c) is about 1.4 Sv between 34.5°S and 20°S and increases to 2.4 Sv at 15°S. Although much larger than the standard deviation of the difference $MOC_{T,S} - MOC$ (gray solid line in Fig. 8c), at 30°S and 34°S the signal-to-noise ratio (ratio of MOC standard deviation to the standard deviation of $MOC_{CPIES} - MOC$) is greater than 2 (Table 4). In contrast, the standard deviation of $Q_{CPIES} - Q$ is about 0.15 PW between 34.5°S and 20°S and jumps to 0.32 PW at 15°S (black dashed line in Fig. 8d) and the signal-to-noise ratio (ratio of Q standard deviation to the standard deviation of $Q_{CPIES} - Q$) is only greater than 1 at 30°S and 34.5°S (Table 4). The correlation between MOC_{CPIES} and MOC is smaller than between $MOC_{T,S}$ and MOC (Fig. 8e). There is, however, a clear preference for higher latitudes, with correlation of approximately 0.9 at 30°S and 34.5°S. Correlations, are significantly lower for MHT, with values around 0.6 at 30°S and 34.5°S (black dashed line in Fig. 8f). Note that MHT derived from MOC_{CPIES} using the empirical relationship between MHT and the MOC discussed in section 3b provides a better estimate of MHT that approaches the skill of $Q_{T,S}$ with correlation of approximately 0.85 at 30°S and 34.5°S (not shown).

The reason why the full trans-basin CPIES array is not as successful as the full T, S array is illustrated by Fig. 9. The top panel shows the dynamic range (temporal maximum minus

the temporal minimum) of OFES geopotential height anomalies relative to 1000 db (solid lines in Fig. 9a). Along each latitude, there are several regions where the range of geopotential height anomalies is very small (e.g., dashed lines show where range equals 3 $m^2\ s^{-2}$ for each latitude). These curves are very similar to the dynamic range of vertical acoustic travel times that would be measured by CPIES, and the low signal areas coincide with regions where the performance of the CPIES methodology is poor in the model. Thus, cross-basin integrations of $v_{g,CPIES}$ will be hampered by these regions of lower skill. Note that the dynamic range of the meridional component of the OFES geostrophic velocity mirrors the curves in Fig. 9a (not shown).

Fig. 9a provides additional information useful for the design of a realistically-sized array. First, the dynamic range is largest at higher latitudes (25°S to 34.5°S), consistent with increased skill of the CPIES array at higher latitudes. Second, the signal is mainly concentrated near the western and eastern boundaries along 34.5°S. The Agulhas ring energy is spread out over a larger area and has moved into the interior for 25°S and 30°S, and as such the variability along these latitudes would be difficult to monitor with a practical number of moorings irrespective of the type of measurement system used. Fig. 9b compares the observed dynamic range of sea surface height anomalies from AVISO from 1992 to 2007 in water deeper than 1000 m. While not precisely the same measurement, the observed longitudinal patterns are very similar to the model dynamic height anomaly patterns, except observed Agulhas ring energy does not extend to 25°S (consistent with Dong et al. 2011; E. Giarolla, personal communication), bolstering the idea that a realistic number of moorings will work better at 34.5°S.

6. Arrays with realistic horizontal resolution

By the various measures described in the previous sections, higher latitudes (in particular 30°S and 34.5°S) were shown to be better for a South Atlantic array comprised of geostrophic-type moorings. Of course instrumenting a trans-basin section with a mooring at every 0.2° of longitude is not feasible; even using CPIES such a dense line of instruments is not reasonable. Given that most of the geopotential height anomaly signal is concentrated near the boundaries along 34.5°S (Fig. 9) and that two small arrays have already been deployed near the boundaries at the nominal latitude of 34.5°S (black stars in Fig. 1a), we test whether realistically-sized arrays could be used to monitor the MOC and MHT along that latitude.

The 34.5°S pilot arrays were primarily established to observe components of South Atlantic circulation (i.e., the boundary currents), but are not yet sufficient for basin-wide integrations of volume and heat transport. When geotrophic-type moorings are deployed within OFES at the pilot array sites, limited information on the western boundary flow and even less information on the eastern boundary flow is captured (Fig. 10b) when compared to the full resolution of the model (Fig. 10a). Likewise only a fraction of the variability is captured with the pilot arrays (compare Fig. 11a,b). Hence, different array configurations of dynamic height moorings or CPIES were tested to determine potential modifications to the pilot arrays (Table 5).

Starting from a uniform 1° degradation of the full array, locations were systematically removed from the interior and the boundaries using MOC and MHT reconstruction skill to determine key locations where instruments should be placed within OFES (e.g., how far they array should extend offshore on the boundaries, how close sites should be to topographic

features). Practical constraints such as keeping the number of sites reasonably small were also considered. It was found to be important to place enough sites on the boundaries to ensure that transport variations were adequately resolved, and to also have some sites near topographic features such as Rio Grande Rise, Mid-Atlantic Ridge, and Walvis Ridge (akin to previous studies by Hirschi et al. 2003; Baehr et al. 2004 in North Atlantic). Results are shown for four of the arrays that were tested. These reduced arrays highlight the importance of the interior sites, the western boundary sites, the eastern boundary sites. Note, similar results were found when the four arrays were deployed within POCM, and only results from the OFES analysis are discussed.

Array 1 consists of five interior sites near topographic features: one west of Rio Grande Rise near 32°W, one on either side of Mid-Atlantic Ridge near 20°W and 12°W and one on either side of the Walvis Ridge near 6°W and 1°E. In addition, Array 1 has a site on each boundary inshore of the existing pilot array instruments. By design, this array produces weak geostrophic flows on the boundaries (Figs. 10c and 11c). Array 2 populates the western boundary with an additional 7 moorings compared with Array 1 (Table 5), and adequately resolves the structure and variability of the Brazil Current and Deep Western Boundary Current (Figs. 10d and 11d). Array 3 populates the eastern boundary with an additional 5 moorings compared with Array 1 (Table 5). Array 3 reproduces the northward flowing Benguela Current and southward return flow to the west of that current, and captures most of Agulhas ring variability (Figs. 10e and 11e). Finally, Array 4 combines Arrays 2 and 3 and has a total of 19 moorings (Figs. 10f and 11f).

Fig. 12 shows the mean bias, errors in the vertical structure and temporal evolution of the Array 1 to 4 reconstructed transports relative to the "true" transports. Note that errors in

the vertical structure are estimated by the standard deviation of the difference between the time mean of the vertically integrated transports, $G_{V,array} - G_V$ and $G_{H,array} - G_H$ (see Fig. 13 for Array 4 vertical structures). There is a marked difference in the skill of the MOC and MHT reconstructions for the four different array configurations (Fig. 12). In the model, the MOC and MHT are strongly correlated with Ekman volume and heat transport. As a result, even Array 1 has some skill (correlation greater than 0.5). However, it poorly represents the vertical structure of mean volume and heat transport (Fig. 12c,d) and the standard deviation of $MOC_{Array\ 1} - MOC$ and $Q_{Array\ 1} - Q$ are large (Fig. 12e,f). Both Arrays 2 and 3 produce negatively and positively biased estimates of the mean transports, respectively, as they primarily observe only one side of the basin (Fig. 12a,b). They do, however, decrease the errors in the vertical structure of mean volume and heat transport and the temporal evolution of the MOC and MHT as evidenced by lowered standard deviations and increased correlations when compared with Array 1. Putting together information from both western and eastern boundaries (Array 4) reduces the biases to -0.7 Sv and -0.13 PW and the errors in the vertical structure drop to about 0.6 Sv and 0.03 PW (Fig. 13). Improvements are made to both the temporal evolution of the reconstructed MOC (standard deviation of $MOC_{Array\ 4} - MOC$ is less than 2 Sv and the correlation exceeds 0.75) and MHT (standard deviation of $Q_{Array\ 4} - Q$ is less than 0.15 PW and the correlation exceeds 0.65). For all four arrays, the MOC and MHT reconstructions have comparable skill whether simulated dynamic height moorings or CPIES are considered (compare gray solid and black dashed lines in Fig. 12), because few sites are located in regions where the CPIES methodology was found to perform poorly (Fig. 9). This suggests that CPIES could be an important component of a South Atlantic MOC and MHT array.

7. Summary and Conclusions

To ascertain whether the MOC and MHT variability observed in the North Atlantic is local or part of a larger-scale pattern of variability and to understand the origins and dynamics of this variability, a trans-basin observing system is needed in the South Atlantic. While producing relatively unbiased estimates of South Atlantic transports is an important goal, an array that can characterize the short-term (seasonal to inter-annual) variability of those transports will provide a crucial benchmark for assessing long-term variations. Two numerical simulations, POCM and OFES, were used to determine a suitable latitude for an *in situ* geostrophic velocity measurement system for the MOC and MHT in the South Atlantic. Along five latitudes, 15°S, 20°S, 25°S, 30°S and 34.5°S, geopotential height anomaly profiles and geostrophic velocities were computed directly from the model T, S profiles (simulating dynamic height moorings) or indirectly from look-up tables (simulating CPIES).

The two models produced consistent estimates of the mean strength of the MOC and MHT with values increasing by 0.8 to 1 Sv and 0.04 to 0.09 PW, respectively, from 34.5°S to 15°S. Due to different model-archival frequencies and eddy-resolving nature of OFES vs. eddy-permitting nature of POCM, the total MOC and MHT variability in OFES significantly exceeded that of POCM. Once high-frequency and semi-annual time scales were removed, both models exhibited strong annual cycles in phase with the Ekman annual cycles. While this finding was at odds with quarterly XBT estimates of the annual cycles of the MOC and MHT along 34.5°S (Baringer and Garzoli 2007; Garzoli and Baringer 2007; Dong et al. 2009), it was consistent with recent daily time series observations from the RAPID/MOCHA array at 26.5°N in the North Atlantic (Kanzow et al. 2010; Johns et al. 2011). Continuous-

in-time measurements are needed to resolve this apparent inconsistency between models and observations, and also to investigate why the annual cycle of geostrophic transports are weak relative to the annual cycle of Ekman transports within models. Despite this disagreement, the linear relationship between the MOC and MHT found in observations (Dong et al. 2009; Johns et al. 2011) was also found for both model simulations.

A trans-basin geostrophic array deployed within in OFES was able to reconstruct the mean MOC and MHT, with biases less than $\pm 0.7\ Sv$ and $\pm 0.07\ PW$ everywhere. In POCM, the geostrophic array was unable to reconstruct the mean MOC and MHT at some latitudes due to weak mean ageostrophic currents on the western boundary. In terms of variability, the idealized geostrophic array accurately reproduced the MOC variability at all five latitudes in both simulations (standard deviation of $MOC_{T,S} - MOC$ smaller than 1 Sv and correlation exceeds 0.9) with a slight preference for higher latitudes. Because MHT reconstruction involved a nonlinear calculation and some temperature fluctuations were uncorrelated with geostrophic currents, there was somewhat less skill in the $Q_{T,S}$ reconstructions. However, such a strong relationship exists between MHT and the MOC, that the correlation between $Q_{T,S}$ and Q was still greater than 0.65 everywhere and it increased with higher latitudes.

A trans-basin array of CPIES was deployed in OFES and compared against the trans-basin geostrophic array which is an idealization of an array of dynamic height moorings (e.g., no mooring motion, measurement errors, instrument drift, or vertical subsampling). The skill of MOC and MHT reconstructions for the CPIES array deployed within OFES was modest from 15°S to 25°S, but approached that of the idealized geostrophic array at 30°S and 34.5°S. This was only true at 34.5°S in POCM (e.g., Table 4). Although these results may be model-dependent, analyses conducted with the high resolution OCCAM simulations also

suggest that a geostrophic velocity measurement system deployed between 32°S and 34.5°S would be successful in reproducing the MOC variability (E. McDonagh and P. Abrahamsen, personal communication).

Through analysis of the dynamic range of the OFES geopotential height anomalies relatively quiescent regions in the interior were identified where the performance of the virtual CPIES was poor, limiting the skill of cross-basin integrations. Most of the OFES geopotential height anomaly signal (as well as the actual observed sea surface height anomaly signal) was found at higher latitudes (25°S, 30°S, and 34.5°S). Of those three latitudes, the signal was only concentrated near the boundaries along 34.5°S suggesting that this latitude is well suited for a realistically-sized South Atlantic array. Preliminary analysis of the first 18 months of data from the western boundary moorings along 34.5°S shows a roughly similar longitudinal pattern of dynamic range to that seen in OFES (not shown).

Reconstructions from four realistically-sized arrays that incorporate sites from the existing pilot arrays along 34.5°S were analyzed in OFES. The largest of the four arrays which consisted of 19 mooring sites (8 on the western boundary, 5 in the interior, and 6 on the eastern boundary) was able to reproduce well the temporal evolution and time-mean vertical structure of the MOC and to a lesser extent the MHT. These four arrays minimally sampled the interior, and as a result, the reconstructions from the simulated dynamic height moorings and CPIES had comparable skill. This suggests that CPIES could be an important component of a more balanced South Atlantic array along 34.5°S.

Any planned South Atlantic trans-basin array will likely consist of a combination of instruments that will be used to directly (dynamic height moorings combined with current meters and bottom pressure recorders) and indirectly (CPIES/PIES) estimate the variability

of the MOC and MHT. Given that there is important mesoscale variability in the South Atlantic, analysis of the mooring data will need to be interpreted in concert with other existing observing systems with better zonal resolution but coarser temporal resolution (e.g., altimetry, cross-basin XBT transects, and ARGO). These multi-platform comparisons will be required to better understand how the volume and heat transports estimated by the trans-basin array are influenced by mesoscale features and variability. For these reasons, the mooring locations should be strategically placed under JASON and Envisat altimetry groundtracks whenever possible (which may also allow some extension of the analysis to the previous decade). What this study has shown is that, so long as enough sites are located on the western and eastern boundaries and in the interior near key topographic features, a trans-basin array of approximately 20 geostrophic-type moorings can be effectively used to reproduce the temporal evolution and vertical structure of the MOC and MHT along the nominal latitude of 34.5°S.

Acknowledgments.

The authors would like to thank Povl Abrahamsen, Yeun-Ho Daneshzadeh, Gustavo Goni, Joel Hirschi, and Bill Johns for helpful discussions regarding the MOC and MHT reconstructions. We thank Shenfu Dong and Tony Lee for the suggestion to explore the dependence of the MOC and MHT relationship on different time scales. Comments from SAMOC3 Workshop participants (http://www.aoml.noaa.gov/phod/SAMOC/) and reviewers improved the manuscript. Thank you to Yoshikazu Sasai, Robin Tokmakian, Corinne James, and Eric Beals for providing output from the OFES and POCM simulations. The AVISO product was produced by the CLS Space Oceanography Division as part of the Environment and Climate EU ENACT project (EVK2-CT2001-00117) and with support from CNES. The authors RCP, SLG, and CSM were supported by the NOAA/Atlantic Oceanographic and Meteorological Laboratory, and RPM acknowledges NSF grants OCE-0726994 and OCE-0928348 and NASA grant NNX08AR40G.

REFERENCES

Baehr, J., J. Hirschi, J.-O. Belsmann, and J. Marotzke, 2004: Monitoring the meridional overturning circulation in the North Atlantic: A model-based array design study. *J. Marine Res.*, **62**, 283-312.

Baehr, J., A. Stroup, and J. Marotzke, 2009: Testing concepts for continuous monitoring of the meridional overturning circulation in the South Atlantic. *Ocean Modelling*, **29**, 147-153.

Baringer, M. O., and S. L. Garzoli, 2007: Meridional heat transport determined with expendable bathythermographs Part I: Error estimates from model and hydrographic data. *Deep Sea Res., I*, **54**, 1390-1401.

Baringer, M. O., and J. C. Larsen, 2001: Sixteen years of Florida current transport at 27°N. *Geophys. Res. Lett.*, **28**, 3179-3182.

Bryden, H. L., H. R. Longworth, and S. A. Cunningham, 2005: Slowing of the Atlantic overturning circulation at 26°N. *Nature*, **438**, 655-657.

Cunningham, S. A., T. Kanzow, D. Rayner, M. O. Baringer, W. E. Johns, J. Marotzke, H. R. Longworth, E. M. Grant, J. J.-M. Hirschi, L. M. Beal, C. S. Meinen, and H. L. Bryden, 2007: Temporal variability of the Atlantic meridional overturning circulation at 26.5°N. *Science*, **317**, 934.5-937. DOI:10.1126/science.1141304

605 Dong, S., S. L. Garzoli, M. O. Baringer, 2011: The role of inter-ocean exchanges on decadal
606 variations of the northward heat transport in the South Atlantic. *J. Phys. Oceanogr.*, in
607 press.

608 Dong, S., S. L. Garzoli, M. O. Baringer, C. S. Meinen, and G. J. Goni, 2009: Interannual
609 variations in the Atlantic meridional overturning circulation and its relationship with the
610 net northward heat transport in the South Atlantic. *Geophys. Res. Lett.*, **36**, L20606,
611 doi:10.1029/2009GL039356.

612 Fetter, A. F. H., and R. P. Matano, 2008: On the origins of the variability of the Malvinas
613 current in a global, eddy-permitting numerical simulation. *J. Geophys. Res.*, **113**, C11018,
614 doi:1029/2008JC004875.

615 Garzoli, S. L., and Baringer, M. O., 2007: Meridional heat transport determined with ex-
616 pendable bathythermographs Part II: South Atlantic transport. *Deep Sea Res., I*, **54**,
617 1402-1420.

618 Garzoli, S. L., and R. P. Matano, 2011: The South Atlantic and the Atlantic meridional
619 overturning circulation. *Deep Sea Research II*, doi:10.1016/j.dsr2.2010.10.063.

620 Garzoli, S. L., S. Speich, A. Piola, and E. Campos, 2010: South Atlantic Meridional Over-
621 turning Circulation (SAMOC) - Third Workshop, *Clivar Exchanges*, No. 54.

622 Ganachaud, A., 2003: Large-scale mass transports, water mass formation, and diffusivi-
623 ties estimated from World Ocean Circulation Experiment (WOCE) hydrographic data. *J.*
624 *Geophys. Res.*, **108**, 3213, doi:10.1029/2002JC001565.

625 Ganachaud, A., and C. Wunsch, 2000: The oceanic meridional overturning circulation, mix-
626 ing, bottom water formation and heat transport. *Nature*, **408**, 453457.

627 Hall, M. M., and H. L. Bryden, 1982: Direct estimates and mechanisms of ocean heat
628 transport. *Deep Sea Res., Part A*, **29**, 339359.

629 Hirschi, J., J. Baehr, J. Marotzke, J. Stark, S. Cunningham, J.-O. Beismann, 2003: A
630 monitoring design for the Atlantic meridional overturning circulation. *Geophys. Res. Lett.*,
631 **30**, 1413, doi:10.1029/2002GL016776.

632 Hogg, N. G., G. Seidler, and W. Zenk, 1999: Circulation and variability at the southern
633 boundary of the Brazil basin. *J. Phys. Oceanogr.*, **29**, 145-157.

634 Johns, W. E., L. M. Beal, M. O. Baringer, J. R. Molina, S. A. Cunningham, T. Kanzow,
635 and D. Rayner, 2008: Variability of shallow and deep western boundary currents off the
636 Bahamas during 200405: Results from the 26.5°N RAPID-MOC Array. *J. Phys. Oceanogr.*,
637 **38**, 605-623.

638 Johns, W. E., M. O. Baringer, L. M. Beal, S. A. Cunningham, T. Kanzow, H. L. Bryden,
639 J. J. M. Hirschi, J. Marotzke, C. S. Meinen, B. Shaw, and R. Curry, 2011: Continuous,
640 array-based estimates of Atlantic ocean heat transport at 26.5°N. *J. Clim.*, **24**, 2429-2449.

641 Jullion, L., K. J. Heywood, A. C. Naveira Garabato, and D. P. Stevens, 2010: Circulation
642 and water mass modification in the Brazil-Malvinas confluence. *J. Phys. Oceanogr.*, in
643 press.

644 Kanzow, T., S. A. Cunningham, W. E. Johns, J. J.-M. Hirschi, J. Marotzke, M. O. Baringer,
645 C. S. Meinen, M. P. Chidichimo, C. Atkinson, L. M. Beal, H. L. Bryden, and J. Collins,

2010: Seasonal variability of the Atlantic meridional overturning circulation at 26.5°N. *J. Climate*, **23**, 5678-5698.

Lee, T., and J. Marotzke, 1998: Seasonal cycles of meridional overturning and heat transport of the Indian Ocean. *J. Phys. Oceanogr.*, **28**, 923-943.

Lumpkin, R., and K. Speer, 2007: Global ocean meridional overturning. *J. Phys. Oceanogr.*, **37**, 2550-2562.

Masumoto, Y., 2010: Sharing the results of a high-resolution ocean general circulation model under a multi-discipline framework a review of OFES activities. *Ocean Dyn.*, **60**, 633-652.

Masumoto, Y., H. Sasaki, T. Kagimoto, N. Komori, A. Ishida, Y. Sasai, T. Miyama, T. Motoi, H. Mitsudera, K. Takahashi, H. Sakuma, and T. Yamagata, 2004: A fifty-year eddy-resolving simulation of the world ocean - preliminary outcomes of OFES (OGCM for the Earth Simulator). *J Earth Simulator*, **1**, 3556.

Matano, R. P., and E. J. Beier, 2003: A kinematic analysis of the Indian/Atlantic interocean exchange. *Deep Sea Res. II*, **50**, 229-249.

Meinen, C. S., and D. R. Watts, 2000: Vertical structure and transport on a transect across the North Atlantic Current near 42°N: time series and mean. *J. Geophys. Res.*, **105 (C9)**, 21 86921 891.

Meinen, C. S., S. L. Garzoli, W. E. Johns, and M. O. Baringer, 2004: Transport variability of the deep western boundary current and the Antilles current off Abaco Island, Bahamas. *Deep Sea Res., I*, **51**, 1397-1415.

Meinen, C. S., M. O. Baringer, and S. L. Garzoli, 2006: Variability in deep western boundary current transports: Preliminary results from 26.5°N in the Atlantic. *Geophys. Res. Lett.*, **33**, L17610, doi:10.1029/2006GL026965.

Priestley, M. B., 1981: Spectral Analysis and Time Series. Academic Press, 890 pp.

Sasaki, H., M. Nonaka, Y. Sasai, H. Uehara, H. Sakuma, 2008: An eddy-resolving hindcast simulation of the quasiglobal ocean from 1950 to 2003 on the Earth Simulator. *High resolution numerical modelling of the atmosphere and ocean*, K. Hamilton and W. Ohfuchi, Eds., Springer, New York, 157-185.

Schouten, M. W., and R. P. Matano, 2006: Formation and pathways of intermediate water in the Parallel Ocean Circulation Models Southern Ocean. *J. Geophys. Res.*, **111**, C06015, doi:10.1029/2004JC002357.

Semtner, A. J., and R. M. Chervin, 1992: Ocean general circulation from a global eddy-resolving model. *J. Geophys. Res.*, **97**, 5493-5550.

Sime, L. C., D. V. Stevens, K. J. Heywood, and K. I. C. Oliver, 2006: A decomposition of the Atlantic meridional overturning. *J. Phys. Oceanogr.*, **36**, 2253-2270.

Speich, S., B. Blanke, and W. Cai, 2007: Atlantic meridional overturning circulation and the Southern Hemisphere supergyre. *Geophys. Res. Lett.*, **34**, L23614, doi:10.1029/2007GL031583.

Stammer, D., R. Tokmakian, A. Semtner, and C. Wunsh, 1996: How well does a 1/4° global circulation model simulate large-scale oceanic observations? *J. Geophys. Res.*, **101**, 25 779-25 812.

687 Tokmakian, R., and P. G. Challenor, 1999: On the joint estimation of model and satellite
688 sea surface height anomaly errors. *Ocean Modelling*, **1**, 39-52.

689 von Storch, J.-S., H. Sasaki, and J. Marotzke, 2007: Wind-generated power input to the
690 deep ocean: an estimate using a 1/10° general circulation model. *J. Phys. Oceanogr.*, **37**,
691 657-672.

692 Watts, D.R., Qian, X., Tracey, K.L., 2001: Mapping abyssal current and pressure fields
693 under the meandering Gulf stream. *J. Atmos. Ocean. Tech.*, **18**, 10521067.

694 Zenk, W., G. Seidler, B. Lenz, and N. G. Hogg, 1999: Antarctic Bottom Water flow through
695 the Hunter Channel. *J. Phys. Oceanogr.*, **29**, 2785-2801.

List of Figures

1 Map of a) POCM and b) OFES twelve-year mean meridional velocity at 200 m depth. Lines indicate the five latitudes tested for a potential South Atlantic array: 15°S, 20°S, 25°S, 30°S, and 34.5°S. Black contours indicate the 100, 1500, 2000, and 3000 m isobaths. Topographic features such as the Rio Grande Rise and the Mid-Atlantic, Walvis, and Vitória-Trindade Ridges are identified in panel a), and the North Brazil, Brazil, and Benguela Currents are identified in panel b). Black stars in panel a) show location of pilot arrays along 34.5°S. Red lines in panel b) delineate approximate boundaries for the Agulhas Eddy corridor. 39

2 Example of virtual IES methodology applied to OFES at 34.5°S, 48°W: a) $\delta(\tau, p)$ look-up table, b) scatter of the actual δ values at 500 db about the δ_{CPIES} values (blue line) as a function of τ, and c) comparison of temporal evolution of Φ (black line) and Φ_{CPIES} (blue line) at 500 db. 40

3 Left panels: MOC time series (in Sv) from the OFES (black line) and POCM (blue line) models at a) 15°S, b) 20°S, c) 25°S, d) 30°S, and e) 34.5°S. Time scales shorter than 9 months have been removed. Right panels: Time-mean of vertically integrated meridional volume transport from $z = 0$ to z, $G_V(z)$, in Sv. See Table 1 for additional statistics. 41

4 MOC variance (upper) and percentage of total variance (lower) partitioned into 5 different frequency bands for OFES (left) and POCM (right) at 15°S (red), 20°S (green), 25°S (blue), 30°S (magenta), and 34.5°S (black). High-frequency (HF), semi-annual (SA), annual (A), inter-annual (IA), and quasi-decadal (QD) bands indicate periods less than 90 days, 90 to 270 days, 270 to 450 days, 450 to 1260 days, and greater than 1260 days, respectively. Circles in panels a) and b) indicate the total unfiltered variance. 42

5 Left panels: Meridional heat transport time series (in PW) from the OFES (black line) and POCM (blue line) models at a) 15°S, b) 20°S, c) 25°S, d) 30°S, and e) 34.5°S. Time scales shorter than 9 months have been removed. Right panels: Time-mean of vertically integrated meridional heat transport from $z = 0$ to z, $G_H(z)$, in PW. See Tables 2 and 3 for additional statistics. 43

6 a-b) Correlation and c-d) the slope of linear regression between MHT and MOC transport in 5 different frequency bands for OFES (left) and POCM (right) at 15°S (red), 20°S (green), 25°S (blue), 30°S (magenta), and 34.5°S (black). High-frequency (HF), semi-annual (SA), annual (A), inter-annual (IA), and quasi-decadal (QD) bands indicate periods less than 90 days, 90 to 270 days, 270 to 450 days, 450 to 1260 days, and greater than 1260 days, respectively. 44

7 Reconstruction statistics for the idealized geostrophic (T, S) array deployed within OFES (black solid line) and POCM (blue solid line) at five latitudes. Left panels correspond to the MOC reconstruction, and right panels correspond to the MHT reconstruction. Shown here are the a-b) reconstructed means (dashed line correspond to mean values in Tables 1 and 2), c-d) mean of $MOC_{T,S} - MOC$ and $Q_{T,S} - Q$, e-f) standard deviation of $MOC_{T,S} - MOC$ and $Q_{T,S} - Q$, g-h) correlation between $MOC_{T,S}$ and MOC and $Q_{T,S}$ and Q. Time scales shorter than 9 months have been removed. 45

8 OFES reconstruction statistics for the idealized geostrophic (T, S) array (gray solid line) and CPIES array (black dashed line) at five latitudes. Left panels correspond to the MOC reconstruction, and right panels correspond to the MHT reconstruction. Shown here are the a-b) mean of $MOC_{array} - MOC$ and $Q_{array} - Q$, c-d) standard deviation of $MOC_{array} - MOC$ and $Q_{array} - Q$, e-f) correlation between MOC_{array} and MOC and Q_{array} and Q. Time scales shorter than 9 months have been removed. 46

9 a) Dynamic range of OFES geopotential height anomalies (in $m^2\ s^{-2}$) along 15°S (red), 20°S (green), 25°S (blue), 30°S (magenta), and 34.5°S (black). b) Dynamic range of AVISO SSHA (in dm). Values only shown where bottom depth exceeds 1000 m. An offset is applied from one latitude to the next (dashed lines show reference value of 3 $m^2 s^{-2}$ (3 dm) for each latitude). The thick horizontal bars indicate regions where bottom depth is shallower than 3500 m. 47

10 OFES mean v_g using density profiles for a) full model resolution, b) the pilot array, c) Array 1, d) Array 2, e) Array 3, and f) Array 4. Topographic features such as the Rio Grande Rise and the Mid-Atlantic and Walvis Ridges are identified in panel a) by the labels A, B, and C, respectively. 48

11 Same as Figure 10 except for standard deviation of v_g. 49

12 OFES reconstruction statistics for the reduced T, S (gray solid line) and reduced CPIES (black dashed line) arrays 1 to 4. Left panels correspond to the MOC reconstruction, and right panels correspond to the MHT reconstruction. Shown here are the a-b) mean of $MOC_{array} - MOC$ and $Q_{array} - Q$, c-d) standard deviation of $G_{V,array} - G_V$ and $G_{H,array} - G_H$ (see Fig. 13), e-f) standard deviation of $MOC_{array} - MOC$ and $Q_{array} - Q$, g-h) correlation between MOC_{array} and MOC and Q_{array} and Q. Time scales shorter than 9 months have been removed. 50

13 A comparison of the OFES a) time-mean vertically integrated meridional volume transport $G_V(z)$ (thin black line) with volume transport from T, S Array 4 $G_{V,TS4}$ (gray solid line) and CPIES Array 4 $G_{V,CPIES4}$ (black dashed line) and b) time-mean vertically integrated meridional heat transport $G_H(z)$ (thin black line) with heat transport from T, S Array 4 $G_{H,TS4}$ (gray solid line) and CPIES Array 4 $G_{H,CPIES4}$ (black dashed line). Units are in Sv and PW, respectively. 51

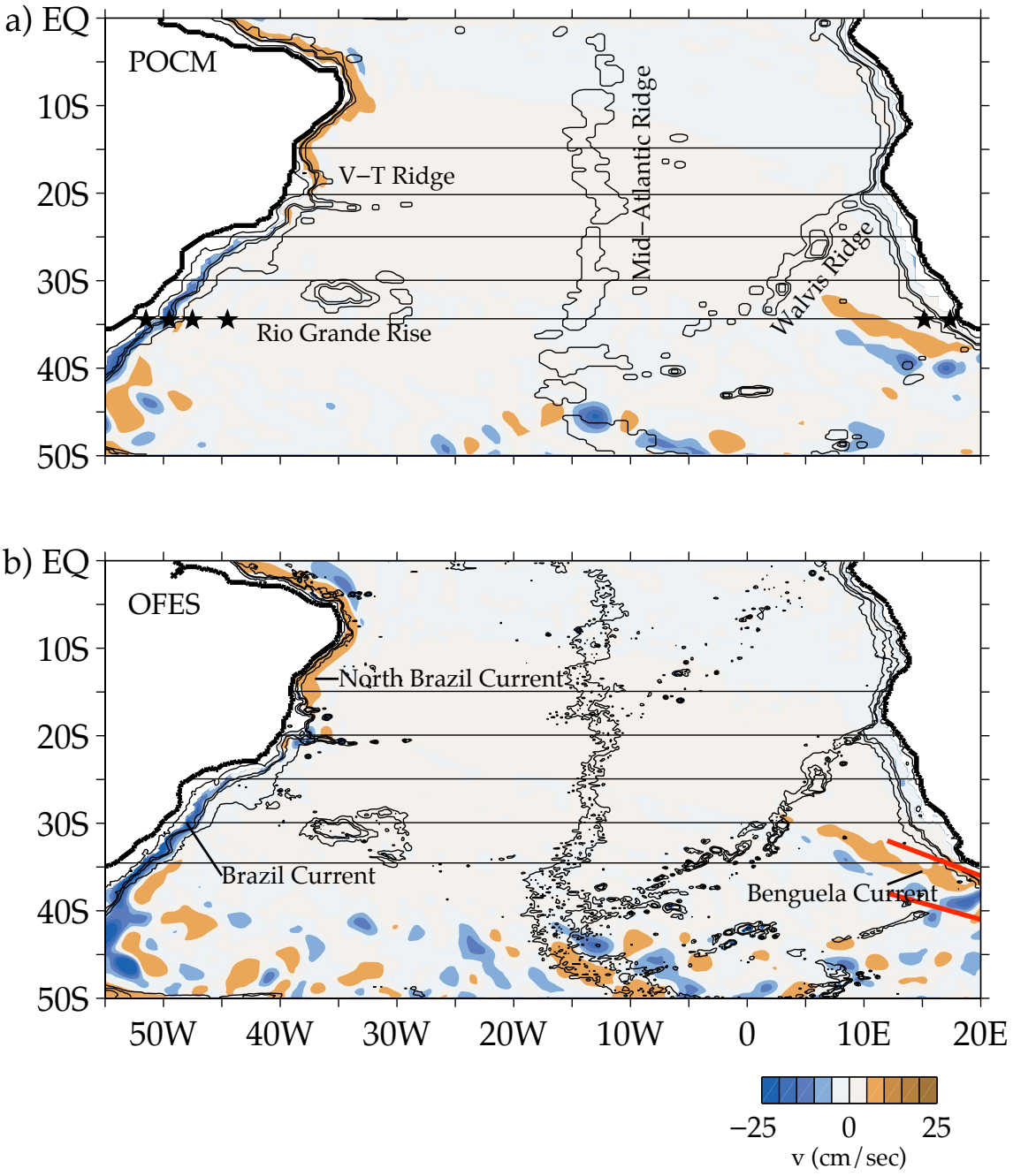

FIG. 1. Map of a) POCM and b) OFES twelve-year mean meridional velocity at 200 m depth. Lines indicate the five latitudes tested for a potential South Atlantic array: 15°S, 20°S, 25°S, 30°S, and 34.5°S. Black contours indicate the 100, 1500, 2000, and 3000 m isobaths. Topographic features such as the Rio Grande Rise and the Mid-Atlantic, Walvis, and Vitória-Trindade Ridges are identified in panel a), and the North Brazil, Brazil, and Benguela Currents are identified in panel b). Black stars in panel a) show location of pilot arrays along 34.5°S. Red lines in panel b) delineate approximate boundaries for the Agulhas Eddy corridor.

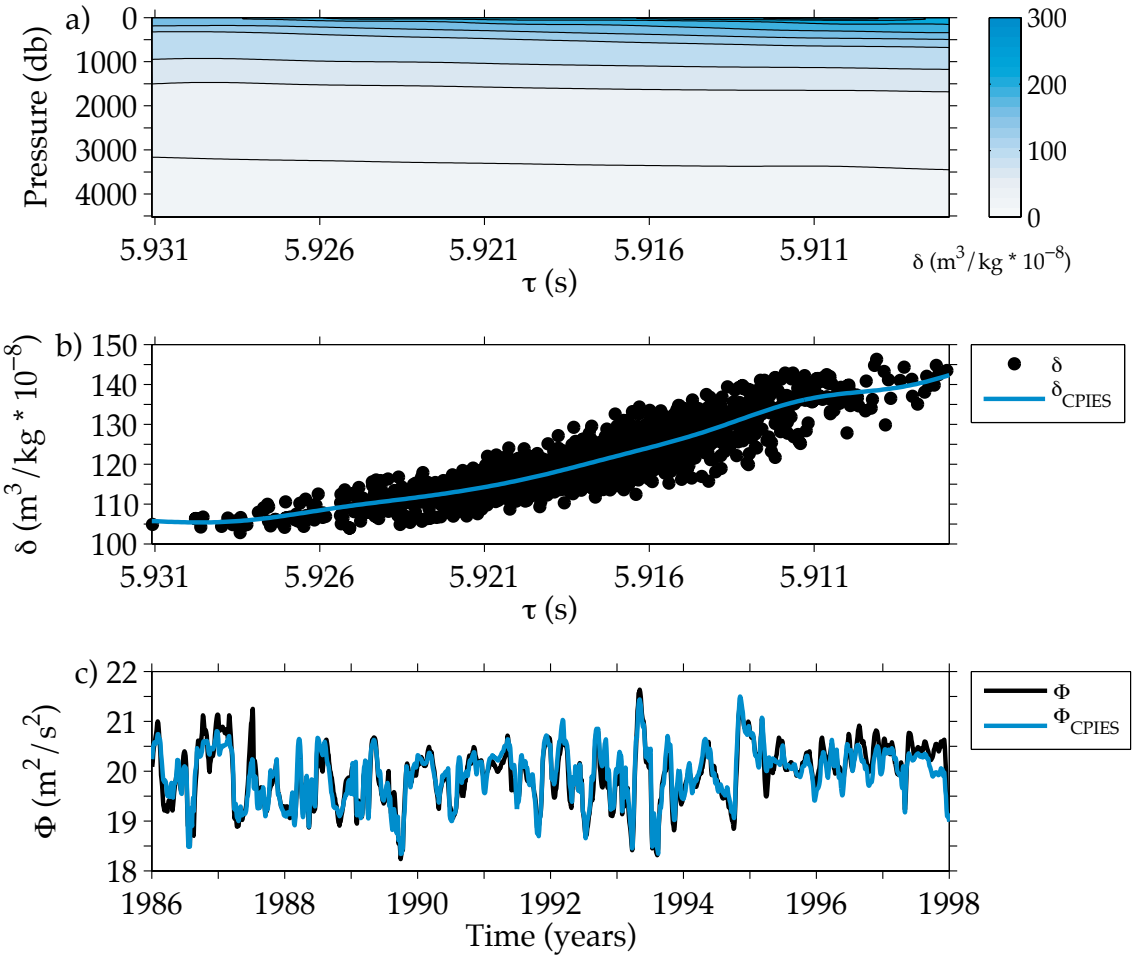

FIG. 2. Example of virtual IES methodology applied to OFES at 34.5°S, 48°W: a) $\delta(\tau, p)$ look-up table, b) scatter of the actual δ values at 500 db about the δ_{CPIES} values (blue line) as a function of τ, and c) comparison of temporal evolution of Φ (black line) and Φ_{CPIES} (blue line) at 500 db.

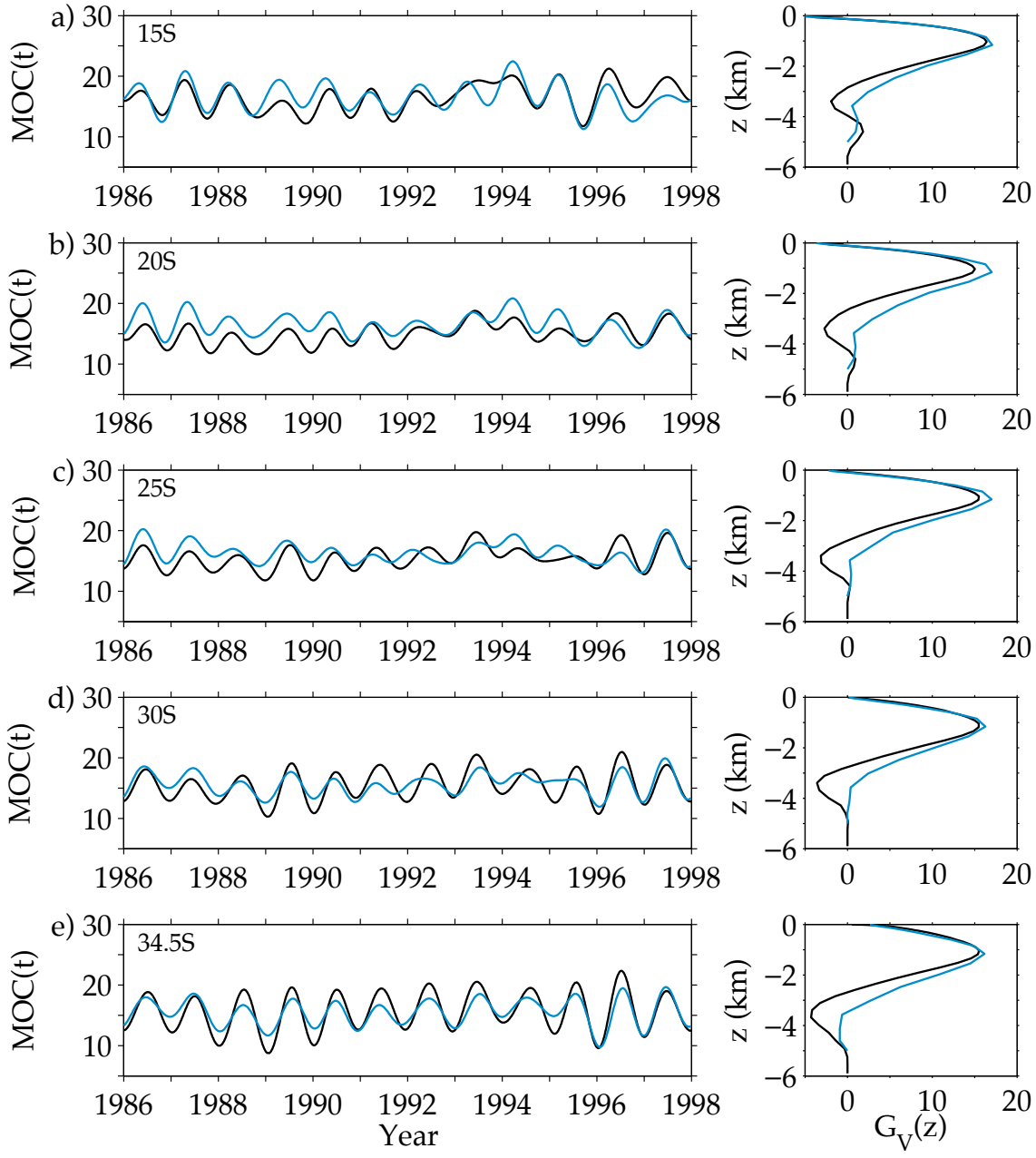

FIG. 3. Left panels: MOC time series (in Sv) from the OFES (black line) and POCM (blue line) models at a) 15°S, b) 20°S, c) 25°S, d) 30°S, and e) 34.5°S. Time scales shorter than 9 months have been removed. Right panels: Time-mean of vertically integrated meridional volume transport from $z = 0$ to z, $G_V(z)$, in Sv. See Table 1 for additional statistics.

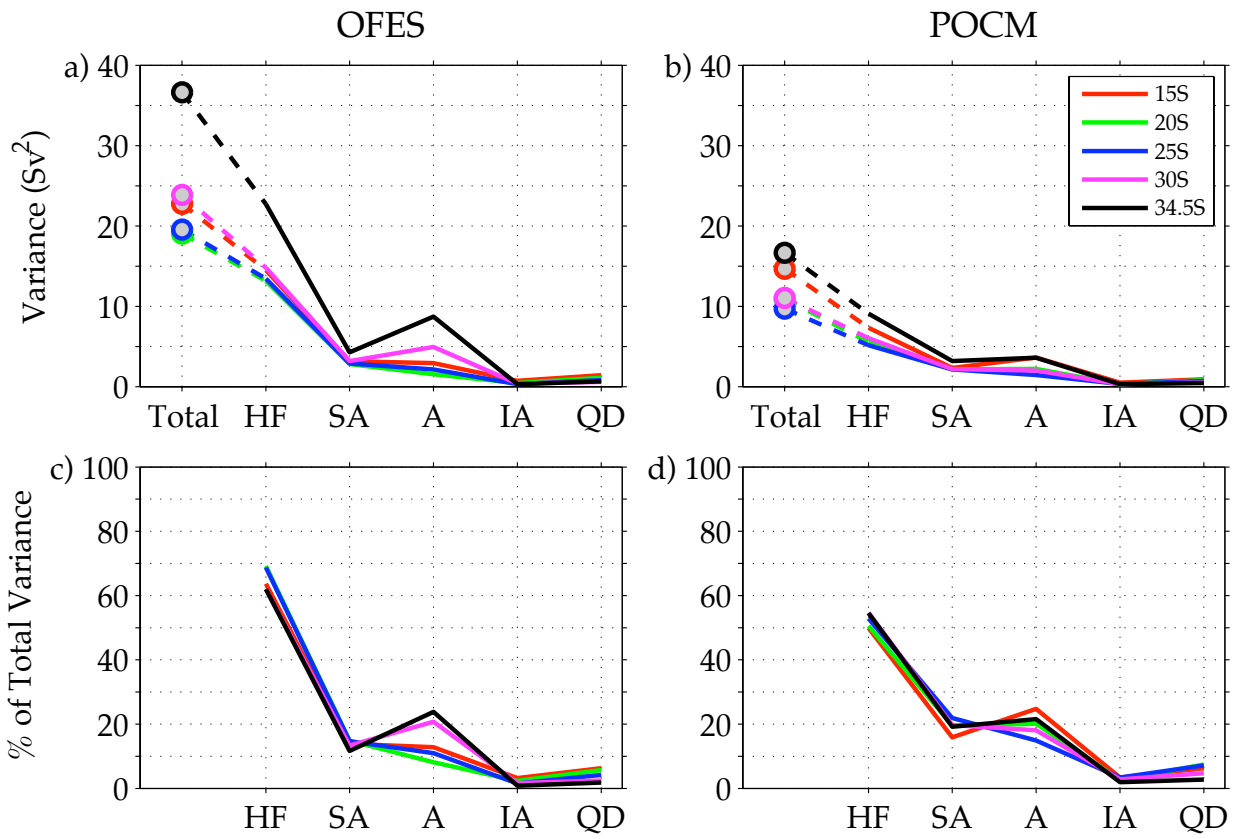

FIG. 4. MOC variance (upper) and percentage of total variance (lower) partitioned into 5 different frequency bands for OFES (left) and POCM (right) at 15°S (red), 20°S (green), 25°S (blue), 30°S (magenta), and 34.5°S (black). High-frequency (HF), semi-annual (SA), annual (A), inter-annual (IA), and quasi-decadal (QD) bands indicate periods less than 90 days, 90 to 270 days, 270 to 450 days, 450 to 1260 days, and greater than 1260 days, respectively. Circles in panels a) and b) indicate the total unfiltered variance.

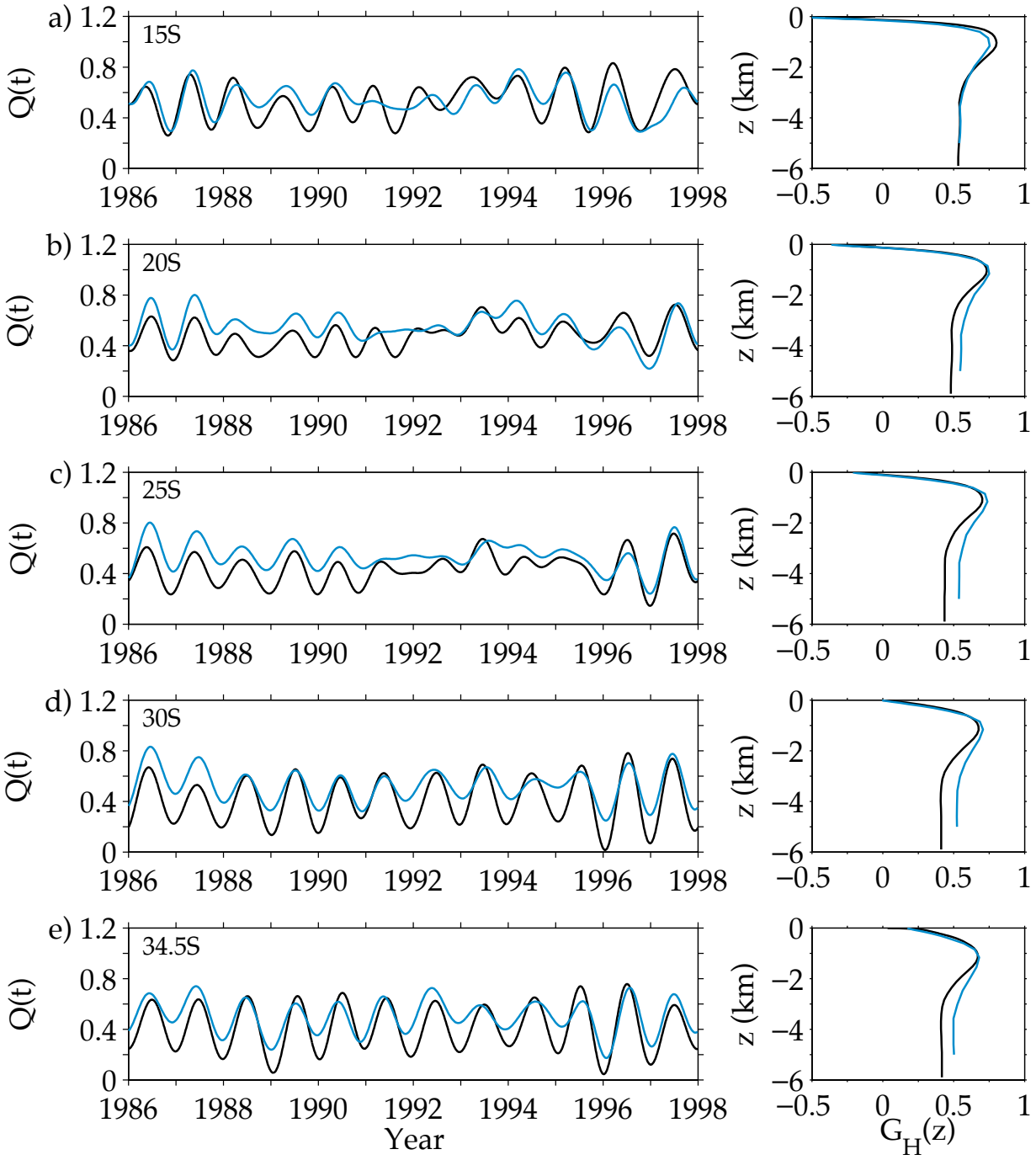

FIG. 5. Left panels: Meridional heat transport time series (in PW) from the OFES (black line) and POCM (blue line) models at a) 15°S, b) 20°S, c) 25°S, d) 30°S, and e) 34.5°S. Time scales shorter than 9 months have been removed. Right panels: Time-mean of vertically integrated meridional heat transport from $z = 0$ to z, $G_H(z)$, in PW. See Tables 2 and 3 for additional statistics.

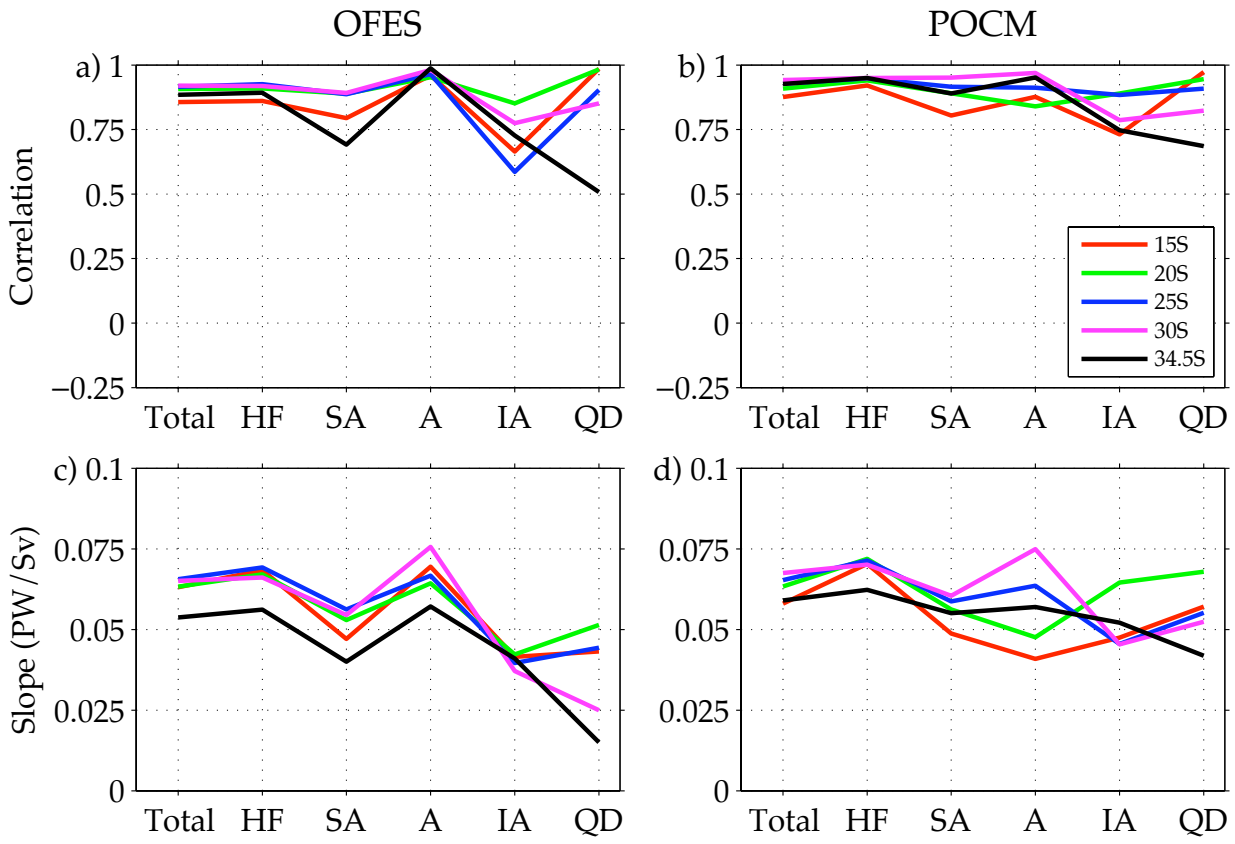

FIG. 6. a-b) Correlation and c-d) the slope of linear regression between MHT and MOC transport in 5 different frequency bands for OFES (left) and POCM (right) at 15°S (red), 20°S (green), 25°S (blue), 30°S (magenta), and 34.5°S (black). High-frequency (HF), semi-annual (SA), annual (A), inter-annual (IA), and quasi-decadal (QD) bands indicate periods less than 90 days, 90 to 270 days, 270 to 450 days, 450 to 1260 days, and greater than 1260 days, respectively.

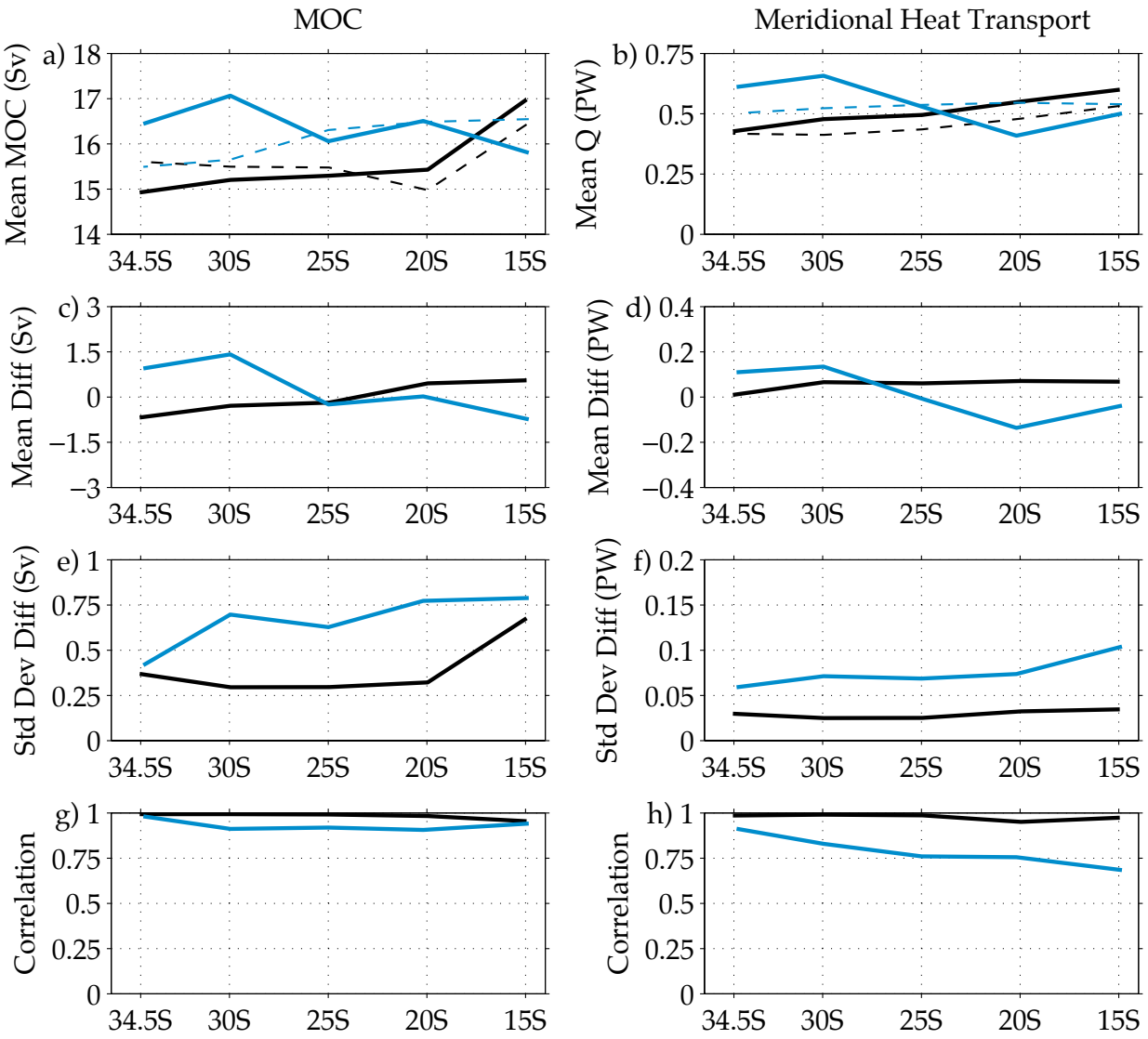

FIG. 7. Reconstruction statistics for the idealized geostrophic (T, S) array deployed within OFES (black solid line) and POCM (blue solid line) at five latitudes. Left panels correspond to the MOC reconstruction, and right panels correspond to the MHT reconstruction. Shown here are the a-b) reconstructed means (dashed line correspond to mean values in Tables 1 and 2), c-d) mean of $MOC_{T,S} - MOC$ and $Q_{T,S} - Q$, e-f) standard deviation of $MOC_{T,S} - MOC$ and $Q_{T,S} - Q$, g-h) correlation between $MOC_{T,S}$ and MOC and $Q_{T,S}$ and Q. Time scales shorter than 9 months have been removed.

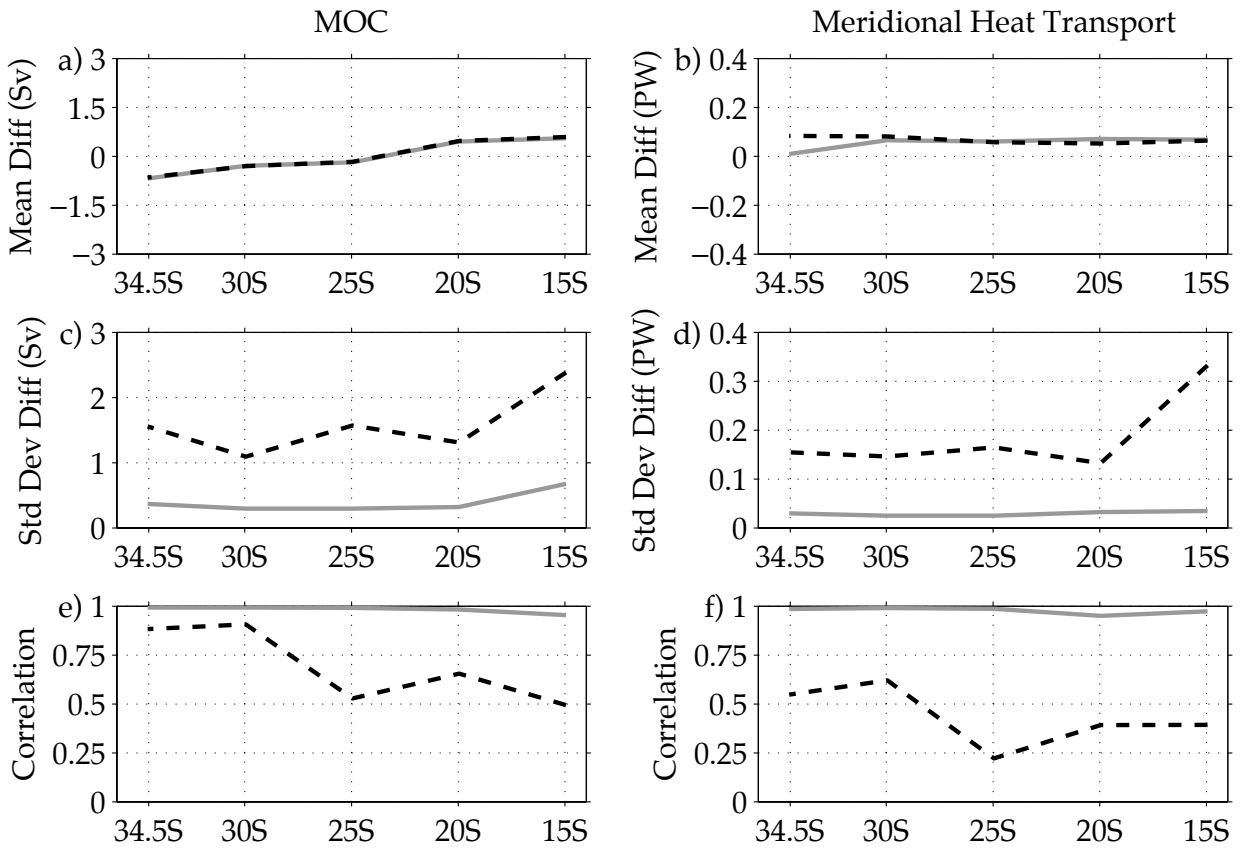

FIG. 8. OFES reconstruction statistics for the idealized geostrophic (T, S) array (gray solid line) and CPIES array (black dashed line) at five latitudes. Left panels correspond to the MOC reconstruction, and right panels correspond to the MHT reconstruction. Shown here are the a-b) mean of $MOC_{array} - MOC$ and $Q_{array} - Q$, c-d) standard deviation of $MOC_{array} - MOC$ and $Q_{array} - Q$, e-f) correlation between MOC_{array} and MOC and Q_{array} and Q. Time scales shorter than 9 months have been removed.

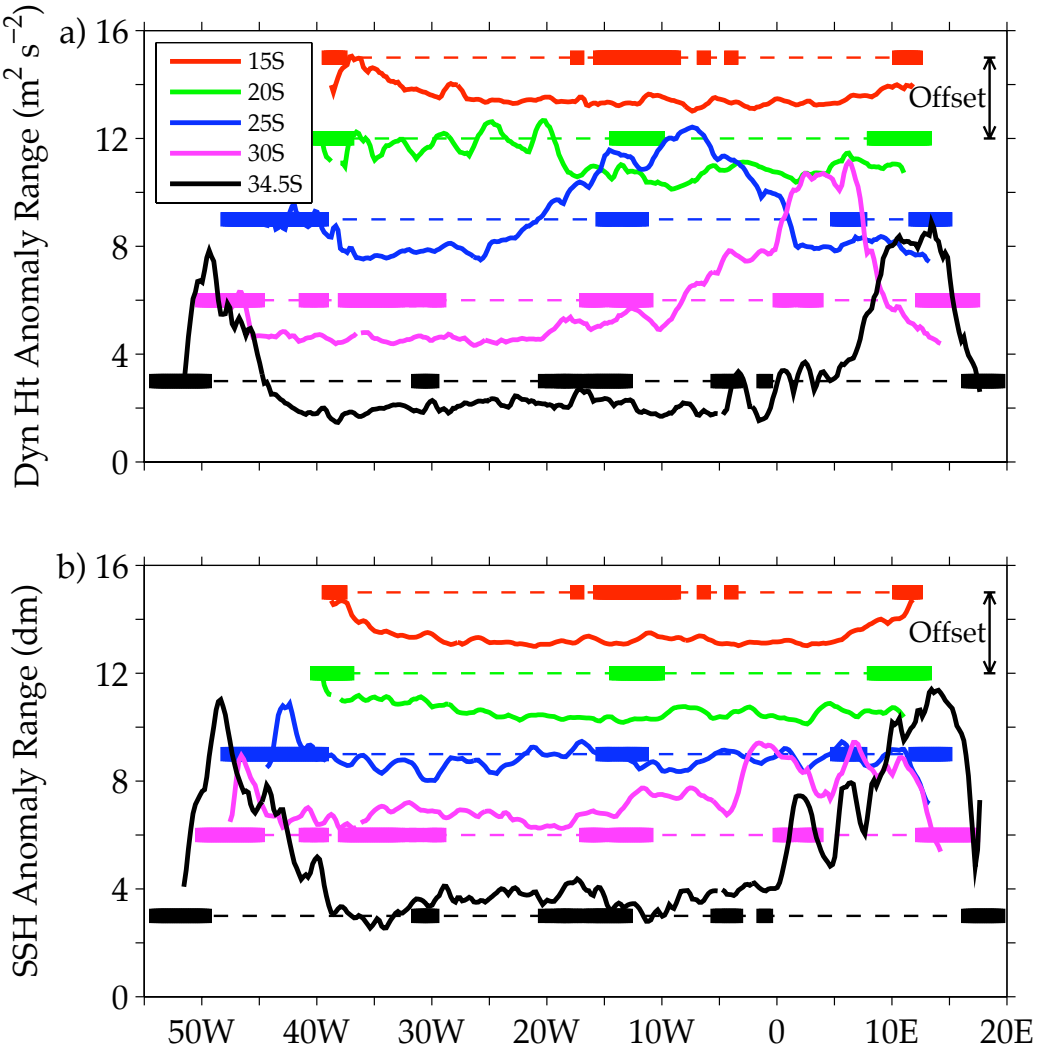

FIG. 9. a) Dynamic range of OFES geopotential height anomalies (in $m^2\ s^{-2}$) along 15°S (red), 20°S (green), 25°S (blue), 30°S (magenta), and 34.5°S (black). b) Dynamic range of AVISO SSHA (in dm). Values only shown where bottom depth exceeds 1000 m. An offset is applied from one latitude to the next (dashed lines show reference value of 3 $m^2 s^{-2}$ (3 dm) for each latitude). The thick horizontal bars indicate regions where bottom depth is shallower than 3500 m.

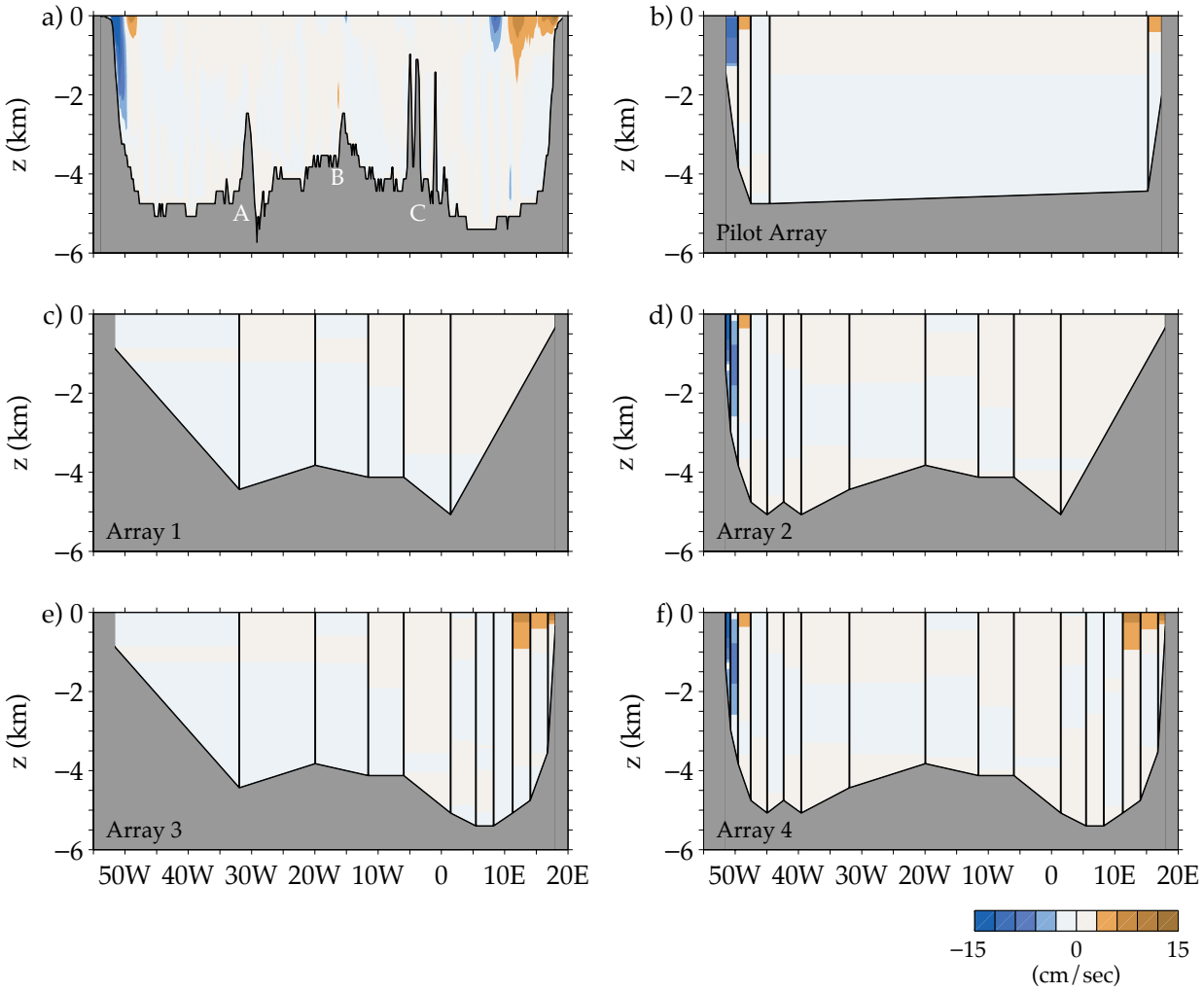

FIG. 10. OFES mean v_g using density profiles for a) full model resolution, b) the pilot array, c) Array 1, d) Array 2, e) Array 3, and f) Array 4. Topographic features such as the Rio Grande Rise and the Mid-Atlantic and Walvis Ridges are identified in panel a) by the labels A, B, and C, respectively.

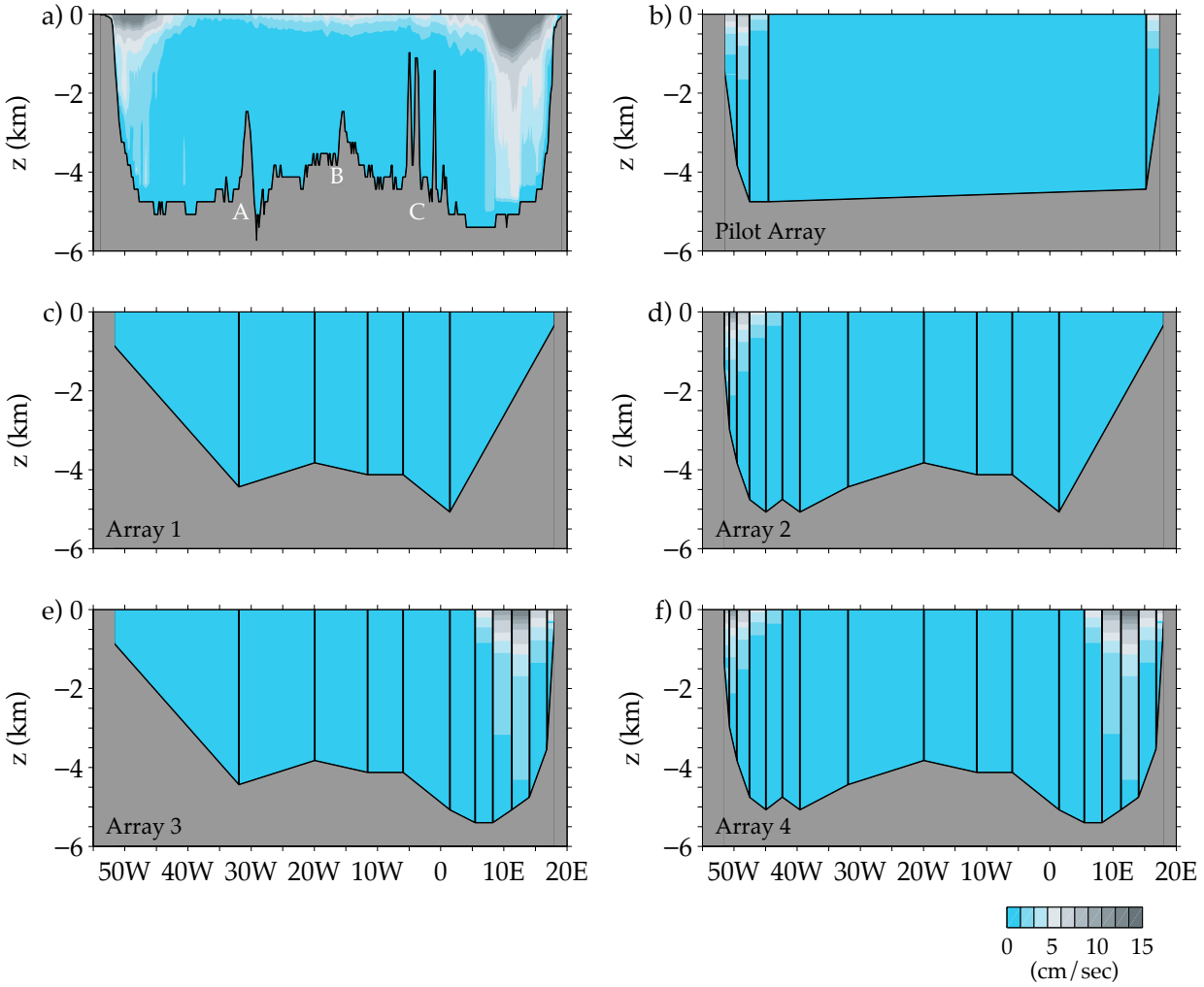

FIG. 11. Same as Figure 10 except for standard deviation of v_g.

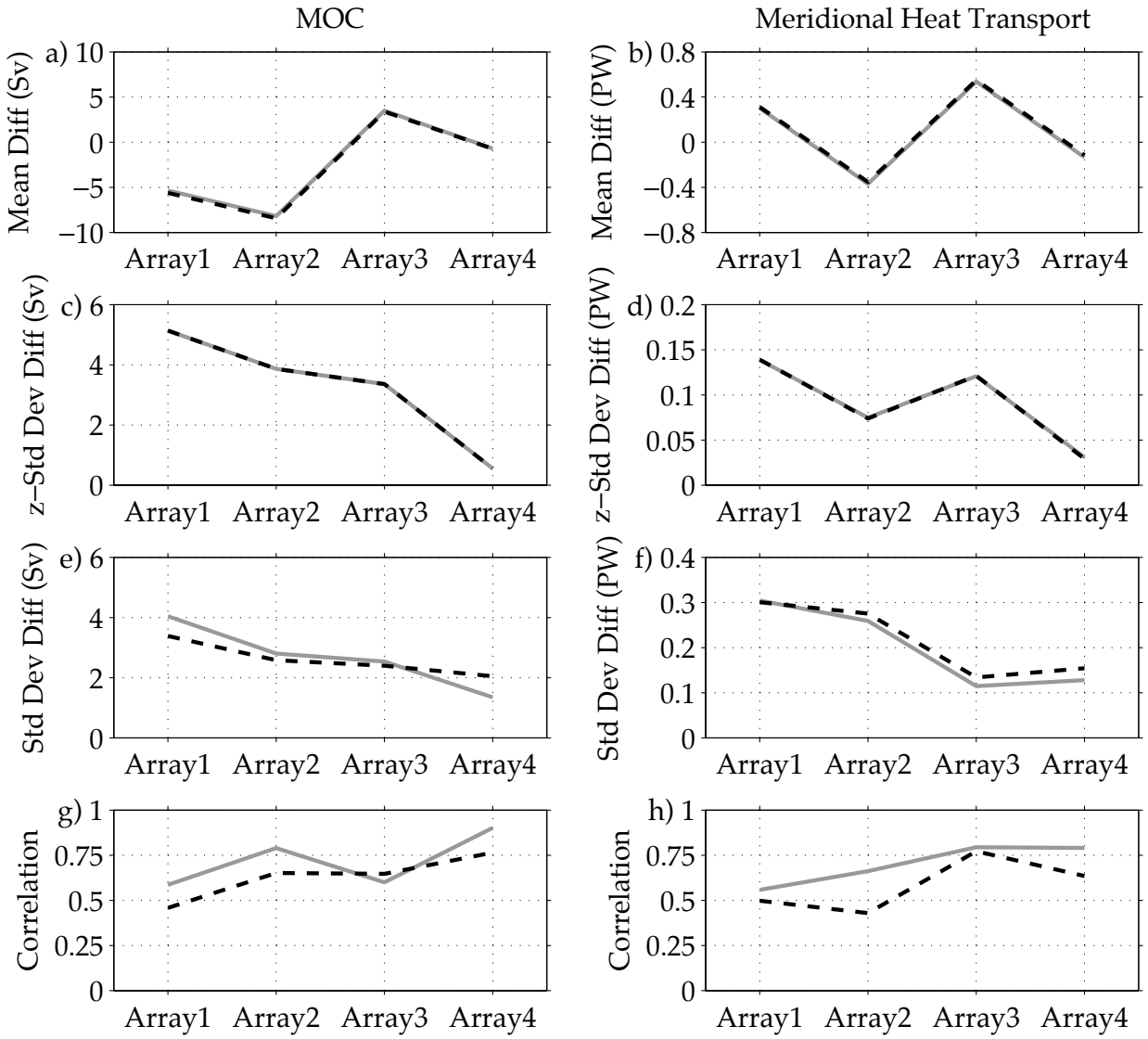

FIG. 12. OFES reconstruction statistics for the reduced T, S (gray solid line) and reduced CPIES (black dashed line) arrays 1 to 4. Left panels correspond to the MOC reconstruction, and right panels correspond to the MHT reconstruction. Shown here are the a-b) mean of $MOC_{array} - MOC$ and $Q_{array} - Q$, c-d) standard deviation of $G_{V,array} - G_V$ and $G_{H,array} - G_H$ (see Fig. 13), e-f) standard deviation of $MOC_{array} - MOC$ and $Q_{array} - Q$, g-h) correlation between MOC_{array} and MOC and Q_{array} and Q. Time scales shorter than 9 months have been removed.

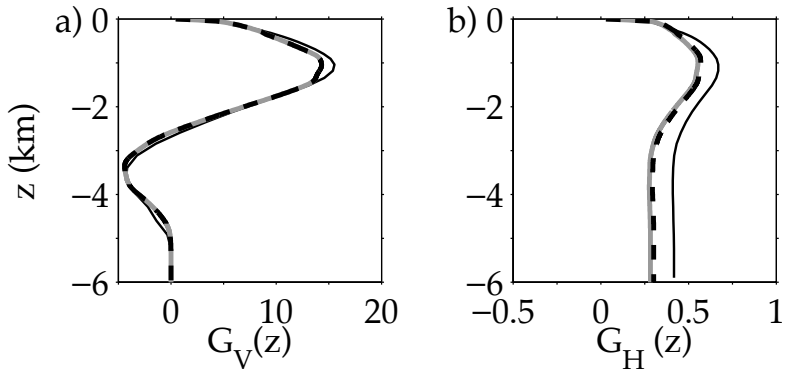

FIG. 13. A comparison of the OFES a) time-mean vertically integrated meridional volume transport $G_V(z)$ (thin black line) with volume transport from T, S Array 4 $G_{V,TS4}$ (gray solid line) and CPIES Array 4 $G_{V,CPIES4}$ (black dashed line) and b) time-mean vertically integrated meridional heat transport $G_H(z)$ (thin black line) with heat transport from T, S Array 4 $G_{H,TS4}$ (gray solid line) and CPIES Array 4 $G_{H,CPIES4}$ (black dashed line). Units are in Sv and PW, respectively.

List of Tables

1 Statistics for OFES (subscript O) and POCM (subscript P) MOC at five latitudes. Mean strength (μ) and standard deviation (σ) of MOC(t), as well as inter-model bias, standard deviation of the difference $MOC_O - MOC_P$, and the correlation between MOC_O and MOC_P. Time scales shorter than 9 months have been removed. 53

2 Statistics for OFES (subscript O) and POCM (subscript P) MHT at five latitudes. Mean strength (μ) and standard deviation (σ) of MHT, as well as inter-model bias, standard deviation of the difference $Q_O - Q_P$, and correlation between Q_O and Q_P. Time scales shorter than 9 months have been removed. 54

3 Correlation (r) and slope (s) of linear regression between MHT and the MOC. Time scales shorter than 9 months have been removed. 55

4 Signal-to-noise (SNR) ratio for the MOC (ratio of standard deviation of MOC to the standard deviation of the difference $MOC_{CPIES} - MOC$) and MHT (ratio of standard deviation of Q to the standard deviation of the difference $Q_{CPIES} - Q$) for OFES and POCM simulations. 56

5 The locations of the pilot array instruments and those of four reduced arrays deployed in OFES along 34.5°S. 57

TABLE 1. Statistics for OFES (subscript O) and POCM (subscript P) MOC at five latitudes. Mean strength (μ) and standard deviation (σ) of MOC(t), as well as inter-model bias, standard deviation of the difference $MOC_O - MOC_P$, and the correlation between MOC_O and MOC_P. Time scales shorter than 9 months have been removed.

Latitude	$\mu_O(Sv)$	$\mu_P(Sv)$	$\sigma_O(Sv)$	$\sigma_P(Sv)$	Bias(Sv)	Std Dev Diff(Sv)	Corr
15°S	16.4	16.5	2.2	2.2	-0.1	1.7	0.71
20°S	15.0	16.5	1.7	1.8	-1.5	1.5	0.66
25°S	15.5	16.3	1.8	1.6	-0.8	1.5	0.63
30°S	15.5	15.7	2.4	1.7	-0.2	1.6	0.76
34.5°S	15.6	15.5	3.1	2.1	-0.1	1.5	0.90

TABLE 2. Statistics for OFES (subscript O) and POCM (subscript P) MHT at five latitudes. Mean strength (μ) and standard deviation (σ) of MHT, as well as inter-model bias, standard deviation of the difference $Q_O - Q_P$, and correlation between Q_O and Q_P. Time scales shorter than 9 months have been removed.

Latitude	$\mu_O(PW)$	$\mu_P(PW)$	$\sigma_O(PW)$	$\sigma_P(PW)$	Bias(PW)	Std Dev Diff(PW)	Corr
15°S	0.53	0.54	0.14	0.11	-0.01	0.10	0.70
20°S	0.48	0.55	0.10	0.11	-0.07	0.09	0.65
25°S	0.43	0.54	0.12	0.10	-0.10	0.07	0.79
30°S	0.41	0.52	0.18	0.12	-0.11	0.09	0.86
34.5°S	0.42	0.50	0.18	0.13	-0.08	0.09	0.86

TABLE 3. Correlation (r) and slope (s) of linear regression between MHT and the MOC. Time scales shorter than 9 months have been removed.

Latitude	r_O	r_P	$s_O(PW/Sv)$	$s_P(PW/Sv)$
15°S	0.91	0.87	0.058	0.044
20°S	0.94	0.87	0.057	0.054
25°S	0.91	0.91	0.060	0.058
30°S	0.95	0.92	0.069	0.068
34.5°S	0.96	0.91	0.054	0.055

TABLE 4. Signal-to-noise (SNR) ratio for the MOC (ratio of standard deviation of MOC to the standard deviation of the difference $MOC_{CPIES} - MOC$) and MHT (ratio of standard deviation of Q to the standard deviation of the difference $Q_{CPIES} - Q$) for OFES and POCM simulations.

Latitude	SNR_{MOC} OFES	SNR_{MOC} POCM	SNR_Q OFES	SNR_Q POCM
15°S	0.9	1.5	0.5	0.6
20°S	1.3	1.2	0.8	0.8
25°S	1.1	1.7	0.7	0.8
30°S	2.2	1.3	1.2	0.8
34.5°S	2.0	2.3	1.2	1.4

TABLE 5. The locations of the pilot array instruments and those of four reduced arrays deployed in OFES along 34.5°S.

Description	Reduced Array	Longitude of Nearest OFES Gridpoint
Pilot Array		51.55°W, 49.55°W, 47.55°W, 44.55°W, 15.25°E, 17.45°E
West1	1,2,3,4	51.75°W
West2-West8	2,4	51.55°W, 50.75°W, 49.75°W, 47.55°W, 45.15°W, 42.35°W, 39.55°W
Int1-Int5	1,2,3,4	31.95°W, 19.95°W, 11.55°W, 5.95°W, 1.25°E
East6-East2	3,4	5.45°E, 8.25°E, 11.25°E, 14.05°E, 16.85°E
East1	1,2,3,4	18.05°E